

The  

---

**MEMS Handbook**

Edited by  
**Mohamed Gad-el-Hak**  
*University of Notre Dame*



**CRC PRESS**

---

Boca Raton London New York Washington, D.C.

# 6

## Liquid Flows in Microchannels

---

**Kendra V. Sharp**  
*University of Illinois at  
Urbana-Champaign*

**Ronald J. Adrian**  
*University of Illinois at  
Urbana-Champaign*

**Juan G. Santiago**  
*Stanford University*

**Joshua I. Molho**  
*Stanford University*

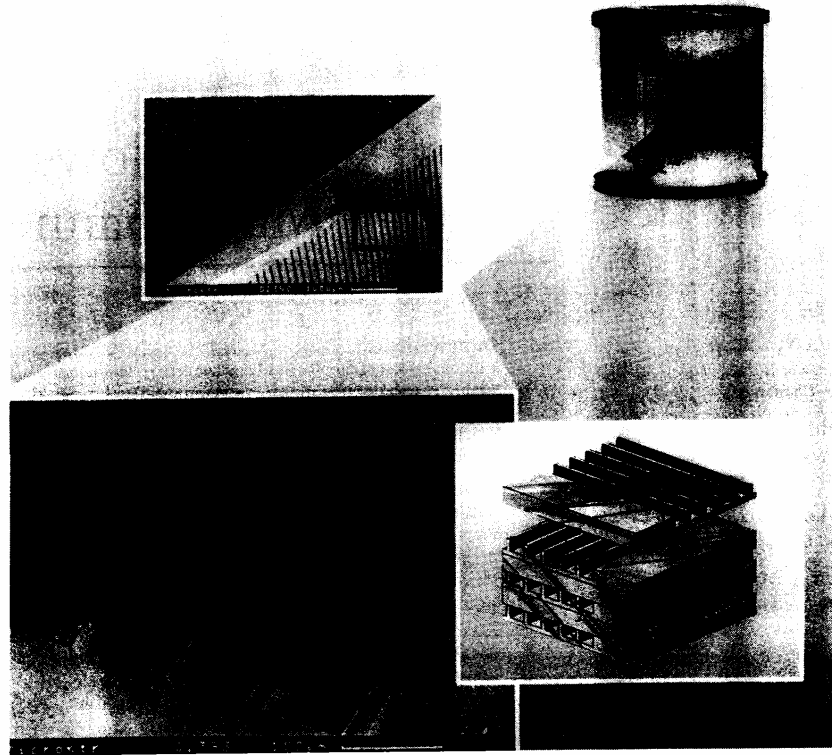
6.1	Introduction .....	6-1
	Unique Aspects of Liquids in Microchannels • Continuum Hydrodynamics of Pressure Driven Flow in Channels • Hydraulic Diameter • Flow in Round Capillaries • Entrance Length Development • Transition to Turbulent Flow • Noncircular Channels	
6.2	Experimental Studies of Flow Through Microchannels .....	6-10
	Proposed Explanations for Measured Behavior • Measurements of Velocity in Microchannels • Nonlinear Channels • Capacitive Effects	
6.3	Electrokinetics Background.....	6-17
	Electrical Double Layers • EOF with Finite EDL • Thin EDL Electro-Osmotic Flow • Electrophoresis • Similarity between Electric and Velocity Fields for Electro-Osmosis and Electrophoresis • Electrokinetic Microchips • Engineering Considerations: Flowrate and Pressure of Electro-Osmotic Flow • Electrical Analogy and Microfluidic Networks • Practical Considerations	
6.4	Summary and Conclusions .....	6-33
	Nomenclature .....	6-33

### 6.1 Introduction

---

Nominally, microchannels can be defined as channels whose dimensions are less than 1 mm and greater than 1  $\mu\text{m}$ . Above 1 mm the flow exhibits behavior that is the same as most macroscopic flows. Below 1  $\mu\text{m}$  the flow is better characterized as nanoscopic. Currently, most microchannels fall into the range of 30 to 300  $\mu\text{m}$ . Microchannels can be fabricated in many materials—glass, polymers, silicon, metals—using various processes including surface micromachining, bulk micromachining, molding, embossing and conventional machining with microcutters. These methods and the characteristics of the resulting flow channels are discussed elsewhere in this handbook.

Microchannels offer advantages due to their high surface-to-volume ratio and their small volumes. The large surface-to-volume ratio leads to a high rate of heat and mass transfer, making microdevices excellent tools for compact heat exchangers. For example, the device in Figure 6.1 is a cross-flow heat exchanger constructed from a stack of 50 14-mm  $\times$  14-mm foils, each containing 34 200- $\mu\text{m}$ -wide  $\times$  100- $\mu\text{m}$ -deep channels machined into the 200- $\mu\text{m}$ -thick stainless steel foils by the process of direct, high-precision mechanical micromachining [Brandner et al., 2000; Schaller et al., 1999]. The direction of flow in adjacent foils is alternated 90°, and the foils are attached by means of diffusion bonding to create a stack of cross-flow heat exchangers capable of transferring 10 kW at a temperature difference of



**FIGURE 6.1** (Color figure follows p. 12-26.) Micro heat exchanger constructed from rectangular channels machined in metal. (Courtesy of K. Schubert and D. Cacuci, Forschungszentrum, Karlsruhe.)

80 K using water flowing at 750 kg/hr. The impressively large rate of heat transfer is accomplished mainly by the large surface area covered by the interior of the microchannel: approximately  $3600 \text{ mm}^2$  packed into a 14-mm cube.

A second example of the application of microchannels is in the area of microelectromechanical systems (MEMS) devices for biological and chemical analyses. The primary advantages of microscale devices in these applications are the good match with the scale of biological structures and the potential for placing multiple functions for chemical analysis on a small area—the concept of a “chemistry laboratory on a chip.”

Microchannels are used to transport biological materials such as (in order of size) proteins, DNA, cells and embryos or to transport chemical samples and analytes. Typical of such devices is the i-STAT blood sample analysis cartridge shown in Figure 6.2. The sample is taken on board the chip through a port and moved through the microchannels by pressure to various sites where it is mixed with analyte and moved to a different site where the output is read. Flows in biological devices and chemical analysis microdevices are usually much slower than those in heat transfer and chemical reactor microdevices.

### 6.1.1 Unique Aspects of Liquids in Microchannels

Flows in microscale devices differ from their macroscopic counterparts for two reasons: the small scale makes molecular effects such as wall slip more important, and it amplifies the magnitudes of certain ordinary continuum effects to extreme levels. Consider, for example, strain rate and shear rate which

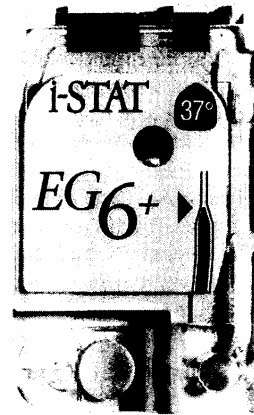


FIGURE 6.2 Blood sample cartridge using microfluidic channels. (Courtesy of i-Stat, East Windsor, NJ.)

scale in proportion to the velocity scale,  $U_s$ , and inverse proportion to the length scale,  $L_s$ . Thus, 100-mm/s flow in a 10- $\mu\text{m}$  channel experiences a shear rate of the order of  $10^4 \text{ s}^{-1}$ . Acceleration scales as  $U_s^2/L_s$ , and is similarly enhanced. The effect is even more dramatic if one tries to maintain the same volume flux while scaling down. The flux scales as  $Q \sim U_s L_s^2$ , so at constant flux  $U_s \sim L_s^{-2}$  and both shear and acceleration go as  $L_s^3$ . Fluids that are Newtonian at ordinary rates of shear and extension can become non-Newtonian at very high rates. The pressure gradient becomes especially large in small cross-section channels. For fixed volume flux, the pressure gradient increases as  $L_s^{-4}$ .

Electrokinetic effects occur at the interface between liquids and solids such as glass due to chemical interaction. The result is an electrically charged double layer that induces a charge distribution in a very thin layer of fluid close to the wall. Application of an electric field to this layer creates a body force capable of moving the fluid as if it were slipping over the wall. The electro-osmotic effect and the electrophoretic effect (charges around particles) will be discussed in detail in a later section. Neither occurs in gases.

The effects of molecular structure are quite different in gases and liquids. If the Knudsen number (defined as  $Kn = \lambda/L_s$ , where  $\lambda$  is the mean free path in a gas and  $L_s$  is the characteristic channel dimension) is greater than  $10^{-3}$  [Gad-el-Hak, 1999; Janson et al., 1999], nonequilibrium effects may start to occur. Modified slip boundary conditions can be used in continuum models for Knudsen numbers between  $10^{-1}$  and  $10^{-3}$  [Gad-el-Hak, 1999]. As the Knudsen number continues to increase, continuum assumptions and fluid theory are no longer applicable. Analysis of such flow requires consideration of different physical phenomena [see Chapter 8 in this book on Analytical and Computational Models for Microscale Flows; Arkilic et al., 1997; Gad-el-Hak, 1999; Harley et al., 1995; Janson et al., 1999].

Because the density of liquids is about 1000 times the density of gases, the spacing between molecules in liquids is approximately ten times less than the spacing in gases. Liquid molecules do not have a mean free path, but following Bridgman (1923), the lattice spacing,  $\delta$ , may be used as a similar measure. The lattice spacing,  $\delta$ , is defined as [Probstein, 1994]:

$$\delta \sim \left( \frac{\bar{V}_1}{N_A} \right)^{1/3} \quad (6.1)$$

where  $\bar{V}_1$  is the molar volume and  $N_A$  is Avogadro's number. For water, this spacing is 0.3 nm. In a 1- $\mu\text{m}$  gap and a 50- $\mu\text{m}$ -diameter channel, the equivalent Knudsen numbers are  $3 \times 10^{-4}$  and  $6 \times 10^{-6}$ , respectively, well within the range of obeying continuum flow. In gases, effects such as slip at the wall occur when the mean free path length of the molecules is more than about one tenth of the flow dimension (i.e., flow

dimensions of order less than 650 nm in air at STP). (Note that the mean free path length of a gas is longer than the mean spacing between its molecules; see Chapter 4 for a detailed discussion.) In liquids, this condition will not occur unless the channels are smaller than approximately 3 nm, and continuum hydrodynamics may provide a useful description at scales even smaller than this because the forces of interaction between molecules in liquids are long range. For example, Stokes' classical result for drag on a sphere is routinely applied to particles whose diameters are well below 100 nm. Thus, liquid flow in microdevices should be described adequately by continuum hydrodynamics well below dimensions of 1  $\mu\text{m}$ .

Molecular effects in liquids are difficult to predict because the transport theory is less well developed than the kinetic theory of gases. For this reason, studies of liquid microflows in which molecular effects may play a role are much more convincing if done experimentally.

Liquids are essentially incompressible. Consequently, the density of a liquid in microchannel flow remains very nearly constant as a function of distance along the channel, despite the very large pressure gradients that characterize microscale flow. This behavior greatly simplifies the analysis of liquid flows relative to gas flows wherein the large pressure drop in a channel leads to large expansion and large changes of thermal heat capacity.

The large heat capacity of liquids relative to gases implies that the effects of internal heating due to viscous dissipation are much less significant in liquid flows. The pressure drop in microchannel flow can be very large, and because all of the work of the pressure difference against the mean flow ultimately goes into viscous dissipation, effects due to internal heating by viscous dissipation may be significant. However, they will be substantially less in liquids than in gases, and they can often be ignored, allowing one to approximate the liquid as a constant density, constant property fluid.

The dynamic viscosity,  $\mu$ , of a liquid is larger than that of a gas by a factor of about 100 (see Table 6.1). This implies much higher resistance to flow through the channels. The kinematic viscosity of a liquid is typically much less than the kinematic viscosity of a gas, owing to the much higher density of liquids (Table 6.1). This implies much more rapid diffusion of momentum in gases. Similar statements pertain qualitatively to the thermal conductivity and the thermal diffusivity.

Liquids in contact with solids or gases have surface tension in the interface. At the microscale, the surface tension force becomes one of the most important forces, far exceeding body forces such as gravity and electrostatic fields.

Bubbles can occur in liquids, for good or ill. Unwanted bubbles can block channels, or substantially alter the flow. But, bubbles can also be used to apply pressure and to perform pumping by heating and cooling the gases inside the bubble.

Particulates and droplets suspended in liquids have densities that match liquid more closely. Settling is much less rapid in liquids, and suspensions have the ability to follow the accelerations of the flow. This effect can also keep suspended impurities in suspension for much longer, thereby increasing the probability that an impurity will introduce unwanted behavior.

Liquids can interact with solids to form an electric double layer at the interface. This is the basis for the phenomena of electro-osmosis and electrophoresis, both of which can be used to move fluid and particles in channels. These topics will be discussed in detail in a later section. Liquids can be non-Newtonian, especially at the high shear rates encountered in microchannels.

TABLE 6.1 Dynamic and Kinematic Viscosities of Typical Liquids Compared to Air at 1 atm

Fluid	Dynamic Viscosity $\mu$ ( $\text{gm cm}^{-1} \text{s}^{-1}$ )	Kinematic Viscosity $\nu$ ( $\text{cm}^2 \text{s}^{-1}$ )	Thermal Conductivity $k$ ( $\text{J K}^{-1} \text{s}^{-1} \text{cm}^{-1}$ )	Thermal Diffusivity $\kappa$ ( $\text{cm}^2 \text{s}^{-1}$ )
Water @15°C	0.0114	0.0114	0.0059	0.00140
Ethyl alcohol @ 15°C	0.0134	0.0170	0.00183	0.00099
Glycerin @15°C	23.3	18.50	0.0029	0.00098
Air @15°C	0.000178	0.145	0.000253	0.202

### 6.1.2 Continuum Hydrodynamics of Pressure Driven Flow in Channels

The general continuum description of the flow of an incompressible, Newtonian fluid flow with variable properties and no body forces other than gravity (i.e., no electrical forces) consists of the incompressible continuity equation:

$$\frac{\partial u_i}{\partial x_j} = 0 \quad (6.2)$$

and the momentum equation:

$$\rho \left( \frac{\partial u_i}{\partial t} + u_j \frac{\partial u_i}{\partial x_j} \right) = \frac{\partial \tau_{ij}}{\partial x_j} + \rho b_i \quad (6.3)$$

where the fluid stress is given by Stokes' law of viscosity:

$$\tau_{ij} = -p\delta_{ij} + \mu \left( \frac{\partial u_i}{\partial x_j} + \frac{\partial u_j}{\partial x_i} \right) \quad (6.4)$$

Here,  $u_i$  is the  $i$ th component of the velocity vector  $\mathbf{u}(\mathbf{x}, t)$ ,  $\rho$  is the mass density ( $\text{kg}/\text{m}^3$ ),  $b_i$  is the body force per unit mass ( $\text{m}/\text{s}^2$ ) (often,  $b_i = g_i$ , the gravitational acceleration), and  $\tau_{ij}$  is the stress tensor ( $\text{N}/\text{m}^2$ ). The corresponding enthalpy equation is

$$\rho c_p \left( \frac{\partial T}{\partial t} + u_j \frac{\partial T}{\partial x_j} \right) = -\frac{\partial q_j}{\partial x_j} + \Phi \quad (6.5)$$

where  $T$  is the temperature, and  $q$  is the heat flux ( $\text{J}/\text{s m}^2$ ) given by Fourier's law of heat conduction by molecular diffusion  $k$ ,

$$q_i = -k \frac{\partial T}{\partial x_i} \quad (6.6)$$

The rate of conversion of mechanical energy into heat due to internal viscous heating is

$$\Phi = \mu \left( \frac{\partial u_i}{\partial x_j} + \frac{\partial u_j}{\partial x_i} \right) \frac{\partial u_i}{\partial x_j} \quad (6.7)$$

Consider a long parallel duct or channel with the  $x$ -direction along the axis of the channel and the coordinates  $y$  and  $z$  in the plane perpendicular to the axis of the channel (Figure 6.3). The entering flow

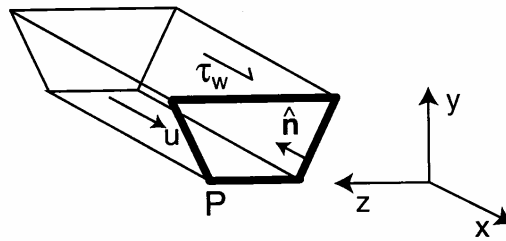


FIGURE 6.3 Flow in a duct of arbitrary cross section  $A$ .  $P$  is the perimeter and  $\tau_w$  is the wall shear stress.

undergoes a transient response in which the velocity and temperature profiles change in the streamwise direction. This process continues until the flow properties become independent of the streamwise position. In this state of fully developed velocity profile, the velocity field is unidirectional,  $\mathbf{u}(x) = (u(y, z), 0, 0)$ , and there is no acceleration of the fluid. Thus, for fully developed flow with gravitational body force  $\mathbf{g}$  the equations become, very simply:

$$\rho \frac{\partial u}{\partial t} = -\frac{dp}{dx} + \rho g_x + \frac{\partial}{\partial y} \left( \mu \frac{\partial u}{\partial y} \right) + \frac{\partial}{\partial z} \left( \mu \frac{\partial u}{\partial z} \right) \quad (6.8)$$

$$\rho c_p \frac{\partial T}{\partial t} = \frac{\partial}{\partial y} \left( k \frac{\partial T}{\partial y} \right) + \frac{\partial}{\partial z} \left( k \frac{\partial T}{\partial z} \right) + \Phi \quad (6.9)$$

Finally, if the flow is steady and the temperature and properties are constant, then the equation for streamwise velocity profiles becomes a simple Poisson equation:

$$\frac{\partial^2 u}{\partial y^2} + \frac{\partial^2 u}{\partial z^2} = \frac{1}{\mu} \frac{d}{dx} (p - \rho g_x x) \quad (6.10)$$

In the absence of electrokinetic effects and for shear rates less than about  $10^{12} \text{ s}^{-1}$ , the appropriate boundary condition is the no-slip condition:

$$u = 0 \quad \text{on the boundary } P \quad (6.11)$$

### 6.1.3 Hydraulic Diameter

Control volume analysis of fully developed flow leads naturally to the concept of the *hydraulic diameter*. Figure 6.3 shows flow in a duct of arbitrary cross section. Because the flow is fully developed and unidirectional (assuming a straight duct), the acceleration is zero and control volume analysis of the momentum reduces to a simple force balance in the streamwise direction,

$$-\frac{dp}{dx} A = \bar{\tau}_w P \quad (6.12)$$

where

$$\bar{\tau}_w = \frac{1}{P} \oint_p \tau_w dl \quad (6.13)$$

is the wall shear stress averaged around the perimeter, and the local wall shear stress is given by:

$$\tau_w = \mu \left. \frac{\partial u}{\partial n} \right|_{n=0} \quad (6.14)$$

Equation (6.12) displays the relevance of the ratio of the area  $A$  to the perimeter  $P$ . In practice, the hydraulic diameter is defined to be

$$D_h = \frac{4A}{P} \quad (6.15)$$

so that when the cross section is a circle,  $D_h$  equals the diameter of the circle. The hydraulic diameter provides a convenient way to characterize a duct with a single length scale and a basis for comparison between ducts of different shapes. A common approximation is to also estimate the flow resistance in a duct or channel as the resistance of a round duct whose diameter is equal to the hydraulic diameter. This approximation is useful but subject to errors of order 10 to 20%. Because solution of Poisson's equation to obtain the exact wall shear stress is accomplished readily by numerical means, it is not necessary.

### 6.1.4 Flow in Round Capillaries

Flow in a round tube is the archetype for all duct and channel flows. While microfabrication characteristically yields channels of noncircular cross section, the round cross section is a useful and familiar point of reference, and microcapillaries are not uncommon. Extensive macroscale research on pipe flows dates back to Hagen's (1839), Poiseuille's (1841) and Reynolds' (1883) original studies in the 19th century. Independently, both Hagen (1839) and Poiseuille (1841) observed the relation between pressure head and velocity and its inverse proportionality to the fourth power of tube diameter.

In a round capillary of radius  $a = D/2$  and radial coordinate  $r$ , it is well known that the velocity profile across a diameter is parabolic:

$$u = u_{\max} \left( 1 - \frac{r^2}{a^2} \right) \quad (6.16)$$

where the maximum velocity is given by:

$$u_{\max} = \frac{a^2}{4\mu} \left( -\frac{dp}{dx} \right) \quad (6.17)$$

The volume flow rate,  $Q$ , is given by:

$$Q = \bar{U}A \quad (6.18)$$

where the average velocity,  $\bar{U}$ , defined by:

$$\bar{U} = \frac{1}{\pi a^2} \int_0^a u(r) 2\pi r dr \quad (6.19)$$

is numerically equal to

$$\bar{U} = \frac{1}{2} u_{\max} \quad (6.20)$$

Using these relations it is easily shown that the pressure drop in a length  $L$ ,  $\Delta p = (-dp/dx)L$ , is given by:

$$\Delta p = \frac{8\mu L Q}{\pi a^4} \quad (6.21)$$

The Darcy friction factor,  $f$ , is defined so that:

$$\Delta p = f \frac{L}{D} \rho \frac{\bar{U}^2}{2} \quad (6.22)$$

(the Fanning friction factor is one fourth the Darcy friction factor). The Reynolds number is defined, in



terms of a characteristic length scale,<sup>1</sup>  $L_s$ , by:

$$Re = \frac{\rho \bar{U} L_s}{\mu} \quad (6.23)$$

For a round pipe, the characteristic length scale is the diameter of the pipe,  $D$ . The friction factor for laminar flow in a round capillary is given by:

$$f = \frac{64}{Re} \quad (6.24)$$

The Poiseuille number is sometimes used to describe flow resistance in ducts of arbitrary cross section. It is defined by:

$$\begin{aligned} Po &= f Re/4 \\ &= -\frac{1}{\mu} \frac{dp}{dx} \frac{D_h^2}{2\bar{U}} \end{aligned} \quad (6.25)$$

where  $L_s$ , used in the calculation of  $Re$  is  $D_h$ . The Poiseuille number has a value of 16 for a round capillary.

The inverse relationship between friction factor and Reynolds number has been well documented on the macroscale. It means that the pressure drop is linearly proportional to the flow rate,  $Q$ . In the laminar region there is no dependence on surface roughness.

As the Reynolds number increases above 2000 in a circular duct, the flow begins to transition to turbulence. At this point, the friction factor increases dramatically, and the flow resistance ultimately becomes proportional to  $Q^2$  rather than  $Q$ .

### 6.1.5 Entrance Length Development

Before the flow reaches the state of a fully developed velocity profile, it must transition from the profile of the velocity at the entrance to the microduct, whatever that is, to the fully developed limit. This transition occurs in the *entrance length* of the duct. In this region, the flow looks like a boundary layer that grows as it progresses downstream. Ultimately, the viscously retarded layers meet in the center of the duct at the end of the entrance length.

The pressure drop from the beginning of the duct to a location  $x$  is given by:

$$p_0 - p(x) = \left( f \frac{x}{D_h} + K(x) \right) \frac{\rho \bar{U}^2}{2} \quad (6.26)$$

where  $K(x)$  is the pressure drop parameter given in Figure 6.4 for a circular duct and for parallel plates [White, 1991]. One sees that the flow development is largely completed by  $x/D = 0.065 Re$ .

### 6.1.6 Transition to Turbulent Flow

In 1883, Reynolds found a critical value of velocity,  $u_{crit}$ , above which the form of the flow resistance changes. The corresponding dimensionless parameter is the critical Reynolds number,  $Re_{crit}$ , below which disturbances in the flow are not maintained. Such disturbances may be caused by inlet conditions such as a sharp edge or unsteadiness in the flow source. Depending on the Reynolds number, disturbances may also be introduced by natural transition to turbulent flow.

<sup>1</sup>In the remainder of this chapter, the characteristic length scale used in calculating  $Re$  is to be inferred from context, e.g., generally  $D_h$  for a rectangular channel and  $D$  for a circular tube.

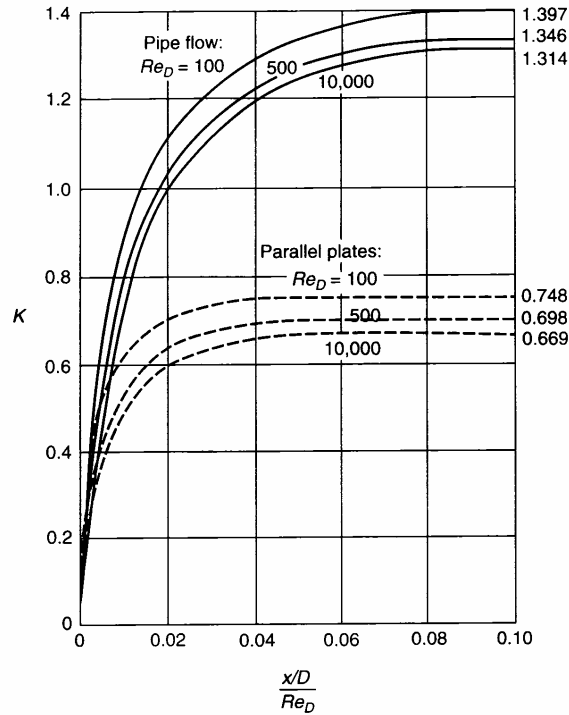


FIGURE 6.4 Entrance length parameter  $K$  for laminar flow in the inlet of a duct. (From White, F.M. (1991) *Viscous Flow*, second edition, McGraw-Hill, New York, p. 292. With permission.)

Reynolds found  $Re_{crit}$  to be approximately 2000, and this value has been generally accepted. Once the flow is fully turbulent, the empirical relationship often used to correlate friction factor and the Reynolds number for smooth pipes and initially proposed by Blasius is

$$f \approx 0.3164 Re^{-0.25} \quad (6.27)$$


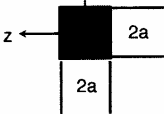
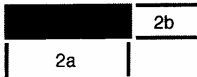


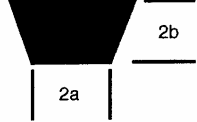
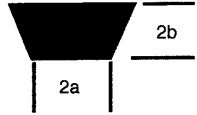
For rough pipes, the friction factor departs from the Blasius relation in the turbulent region. This departure occurs at different values of  $Re$  depending on the magnitude of the surface roughness. The Moody chart summarizes the traditional friction factor curves and is readily available in any basic fluids textbook (e.g., White, 1994, p. 318).

### 6.1.7 Noncircular Channels

Fully developed flow in noncircular ducts is found by solving the Poisson equation (Eq. 6.10). Frequently, analytical solutions can also be found, but the numerical approach is so reliable that there is little need for exact solutions. Developing flow in the entrance region is more difficult, but here again numerical approaches are relatively straightforward. Table 6.2 summarizes the flow resistance for various laminar flows. One sees that the effect of the shape of the channel is relatively weak.

As mentioned earlier, a common approximation made in analyzing flow in ducts of noncircular cross section is to use the results for circular ducts, but with the hydraulic diameter of the noncircular duct replacing that of the round duct. For example, this can be done to estimate the flow resistance of fully developed flow and the resistance in the entrance region.

**TABLE 6.2** Resistance to Flow in Fully Developed Flow Through Straight Microchannels of Various Cross-Sectional Geometries

Cross Section	$f Re$	$u_{max}/u_B$
	64	2.000
	56.92	2.0962
	$96 [ 1 - 1.3553\alpha + 1.9467\alpha^2 - 1.7012\alpha^3 + 0.9564\alpha^4 - 0.2537\alpha^5 ]$	—
$\alpha = b/a$		
	96	1.5000
	60	—
	$\frac{2b/2a}{4.000 \quad 55.66}$ 2.000 55.22 1.000 56.60 0.500 62.77 0.250 72.20	2.181 2.162 2.119 1.969 1.766
	1.000 56.15	2.137

Source: Data from Shah, R.K., and London, A.L. (1978) *Advances in Heat Transfer*, Suppl. 1, Academic Press, New York.

## 6.2 Experimental Studies of Flow Through Microchannels

Despite the fundamental simplicity of laminar flow in straight ducts, experimental studies of microscale flow have often failed to reveal the expected relationship between the friction factor and Reynolds number. Further, flow discrepancies are neither consistently higher nor lower than macroscale predictions. A summary of the experiments that have been conducted to investigate the behavior of fluid flow in microchannels, over a large range of Reynolds numbers, geometries and experimental conditions, is presented in Table 6.3. In reviewing these results, they will be grouped according to the results of friction factor measurements (follow macroscale predictions, higher than predictions, and lower than predictions).

The first experimental investigations of flow through microchannels in the early 1980s were motivated by the interest in high-performance heat sinking. The large surface-to-volume ratios of microchannels make them excellent candidates for efficient heat transfer devices, as discussed in the introduction to this chapter. Tuckerman and Pease (1981) studied flow through an array of microchannels with approximately rectangular cross sections (height range 50 to 56  $\mu\text{m}$ , width range 287 to 320  $\mu\text{m}$ ). Although this study was focused primarily on heat transfer characteristics, they “confirmed that the flow rate obeyed

TABLE 6.3 Experimental Conditions for Flow Resistance Experiments

Study	Working Fluid	Channel Description	Reynolds Numbers
Choi et al. (1991)	Nitrogen gas	Circular: diameter 3–81 $\mu\text{m}$	~30–20,000
Flockhart and Dhariwal (1998)	Water	Trapezoidal: depth 27–63 $\mu\text{m}$ , width 100–1000 $\mu\text{m}$ , length 12–36 mm	<600
Jiang et al. (1995)	Water	Circular: diameter 8–42 $\mu\text{m}$ ; rectangular, trapezoidal and triangular: depth 13.4–46 $\mu\text{m}$ , width 35–110 $\mu\text{m}$ , length 2.5–10 mm	Circular: < ~1.2; unclear for other geometries
Mala and Li (1999)	Water	Circular: diameter 50–254 $\mu\text{m}$	Up to 2500
Papautsky et al. (1999a)	Water	Array of rectangular channels, each: depth 30 $\mu\text{m}$ , width 600 $\mu\text{m}$ , length 3 mm	1–18
Papautsky et al. (1999b)	Water	Rectangular array of channels: height 22.71–26.35 $\mu\text{m}$ , width 150–600 $\mu\text{m}$ , length 7.75 mm	0.001–10
Peng et al. (1994)	Water	Rectangular: height 100–300 $\mu\text{m}$ , width 200–400 $\mu\text{m}$ , length 50 mm	50–4,000
Pfahler et al. (1991)	<i>n</i> -Propanol, silicone oil, nitrogen gas, helium gas	Rectangular and trapezoidal, depending on channel: depth 0.48–38.7 $\mu\text{m}$ , width 55–115 $\mu\text{m}$ , length 10.2–10.9 mm	Liquids: <<1 to approx. 80
Qu et al. (2000)	Water	Trapezoidal: depth 28–114 $\mu\text{m}$ , width 148–523 $\mu\text{m}$ , length 28 mm	~10–1,450
Sharp et al. (2000)	Water	Circular: diameter 75–242 $\mu\text{m}$	50–2500
Tuckerman and Pease (1981)	Water	Array of etched rectangular/ trapezoidal, each: depth 50–56 $\mu\text{m}$ , width 287–320 $\mu\text{m}$ , length 1 cm	~200–600
Wilding et al. (1994)	Water, biological fluids	Trapezoidal: depth 20–40 $\mu\text{m}$ , width 40–150 $\mu\text{m}$ , length 11.7 mm	Water: 17–126
Wu and Little (1983)	Nitrogen, helium and argon	Trapezoidal or U-shaped: depth 28–65 $\mu\text{m}$ , width 133–200 $\mu\text{m}$ , length 7.6–40.3 mm	~200–15,000
Yu et al. (1995)	Nitrogen gas, water	Circular: diameter 19–102 $\mu\text{m}$	250–20,000

Note: When a range of values for channel dimension is given, it indicates that several channels were used, with different individual dimensions.

Poiseuille's equation." Shortly thereafter, a study of microchannels for use in small Joule–Thomson refrigerators was performed [Wu and Little, 1983]. Significant roughnesses were present in some of these etched silicon or glass channels, but friction factors measured in the smoothest channel showed reasonable agreement with theoretical macroscale predictions. Several other experiments have also shown general agreement with macroscale theoretical predictions for friction factor, in at least certain parameter ranges [Flockhart and Dhariwal, 1998; Jiang et al., 1995; Sharp et al., 2000; Wilding et al., 1994].

Geometrical differences were emphasized in Jiang et al.'s (1995) experiments, which employed circular glass microchannels and silicon microchannels with rectangular, trapezoidal and triangular cross sections. Although linear relationships between flow rate and pressure drop were observed in all the microchannels, a direct analysis of the friction factor was not performed except in the case of the circular microchannels ( $D = 8\text{--}42 \mu\text{m}$ ,  $Re < 1.2$ ). In the circular case, the friction factor matched theoretical predictions to within 10 to 20%.

Focusing primarily on biological fluids, but also using water and saline as working fluids, Wilding et al. (1994) found that results for water flowing in silicon micromachined channels (Reynolds numbers ~17 to 126) agreed well with theory for at least the lower Reynolds numbers tested. The disagreement at higher Reynolds numbers was noted to be a result of "entrance effects and inertial losses" not included in the theory.

Saline was also used as the working fluid without much change in the results, suggesting that surface charge effects are minimal. Biological fluids, as expected, exhibited shear thinning and non-Newtonian behavior.

Comparison of numerical calculations for flow in trapezoidal channels finds good agreement between numerics and experiment for  $Re < 600$ , although some entrance effects were observed in the shortest channels [Flockhart and Dhariwal, 1998]. The numerical calculations were motivated by the fact that this particular trapezoidal geometry is very common in microfluidic applications as a result of anisotropic etching techniques employed in fabrication, particularly in  $\langle 100 \rangle$  silicon.

Microscale measurements of the friction factor by Sharp et al. (2000) generally agree with the macroscale laminar theory to within  $\pm 2\%$  experimental error over all Reynolds numbers up to transition ( $-50 < Re < 2000$ ), for water flowing through circular fused silica microchannels with  $D = 75$  to  $242 \mu\text{m}$ . Similar agreement is also obtained using a 20% solution of glycerol and 1-propanol. Occasional discrepancies that fall outside of the error bars tend to occur in the Reynolds number range  $1200 < Re < 2000$ , but in no case is the discrepancy greater than +4%.

Studies finding an increase in friction factor on the microscale under certain conditions include Wu and Little (1983), Peng et al. (1994), Mala and Li (1999), Qu et al. (2000) and Papautsky et al. (1999a; 1999b). In some cases, the departure from agreement with theoretical predictions is reasonably linked with a change in roughness or geometrical parameter. For example, Wu and Little's (1983) friction factor measurements appear to correlate with surface roughness, as the results agreed well with theory for smooth channels, but the agreement decreased as the roughness increased. In the rougher channels (absolute roughness up to  $40 \mu\text{m}$ ), the measured friction factors were higher than theoretical predictions. A linear relationship between  $f$  and  $Re$  was maintained in the laminar region, and the authors suggested that a transition to turbulence appeared at  $Re$  lower than expected (namely, 400) for the roughest glass channel.

In an effort to understand the influence of geometrical parameters (specifically, hydraulic diameter and aspect ratio) on flow resistance, Peng et al. (1994) considered water flows in rectangular machined steel grooves enclosed with a fiberglass cover. A large range of  $Re$  were obtained (50 to 4000), and a geometrical dependence was observed. For the most part,  $f$  increased with increasing  $H/W$  and also with increasing  $D_h$  (holding  $H/W$  constant).

The friction factor was observed to be higher than macroscale predictions for five of seven geometrical cases, all except  $H/W = 0.5$ . Because the relationship between  $f$  and  $Re$  no longer appeared inversely proportional, new power laws were suggested for this correlation in the laminar and turbulent regions, namely,  $f \propto Re^{-1.98}$  and  $f \propto Re^{-1.72}$ , respectively.

In addition to proposing new correlations in the laminar and fully turbulent regions, Peng et al. (1994) suggested that the regions themselves must be redefined depending upon the geometry of the microchannel. As in macroscale flows (*cf.* standard Moody chart, White, 1994, p. 318), two distinct relationships between  $f$  and  $Re$  were observed, one in the lower  $Re$  region and one in the higher  $Re$  region. The area between the two trends represents the transition region. The critical Reynolds number,  $Re_{crit}$  (the  $Re$  above which the low  $Re$  linear trend is no longer appropriate), exhibits a dependence on the hydraulic diameter.  $Re_{crit}$  was estimated at 200 for  $D_h < 220 \mu\text{m}$ , 400 for  $D_h = 240 \mu\text{m}$  and 700 for  $260 < D_h < 360 \mu\text{m}$ , implying, according to Peng et al. (1994), the occurrence of "early transition to turbulence" in these microchannels.

A second study of the dependence on geometrical parameters, but for much smaller  $Re$  ( $-0.001$  to  $10$ ), measured friction factors generally higher than macroscale theory [Papautsky et al., 1999b], more so for the smallest  $Re$  ( $< 0.01$ ). As the Reynolds number increased to  $10$ , the measured friction factor neared the theoretical macroscale predictions, though it still remained up to 20% high, even considering experimental error. A possible dependence of friction characteristics due to size was observed at a small aspect ratios ( $< 0.2$ ), although the authors were not able to attribute this independently to either the small dimension required for small aspect ratio ( $O, 20$  to  $40 \mu\text{m}$ ) or very low Reynolds number.

Nonlinear trends between pressure drop and flowrate were observed for  $Re$  as low as 300 by Mala and Li (1999), specifically for water flowing through a  $130\text{-}\mu\text{m}$ -diameter stainless steel microtube. At small Reynolds numbers ( $Re < 100$ ) the measured friction factors were in "rough agreement" with conventional theory, but for all other  $Re$  (up to 2500), the friction factors were consistently higher in stainless steel and fused silica microtubes (circular cross section). Measured flow friction for trapezoidal

channels was 8 to 38% higher than macroscale predictions for the range of parameters studied by Qu et al. (2000), and a dependence on  $D_h$  and  $Re$  was also observed.

Another group of studies found the flow resistance to be less than theoretical macroscale predictions for certain conditions [Choi et al., 1991; Peng et al., 1994; Pfahler et al., 1990a; 1990b; 1991; Yu et al., 1995]. In the study of geometrical effects by Peng et al. (1994), the friction factor was found to be lower than the macroscale theoretical prediction for two out of seven cases, namely, when  $H/W = 0.5$ . A clear trend between  $Re_{crit}$  and aspect ratio was observable. Although previously described, the trends between friction factor behavior and aspect ratio or hydraulic diameter were less consistent.

Comparing the friction factors for flow through channels with several fluids (2-propanol, *n*-propanol and silicone oil), Pfahler et al. (1990a; 1990b; 1991) found the measured friction factors to be lower than theoretical values for all but two cases: a small depth and very low  $Re$  ( $0.8 \mu\text{m}$ ,  $Re \ll 1$ ) case and the case with largest depth ( $\sim 40 \mu\text{m}$ ). The authors acknowledged that their results depend heavily on channel size measurement, which was extremely difficult to measure accurately for the shallowest channels (depth  $< 1 \mu\text{m}$ ). The Reynolds numbers in their liquid flow experiments varied from much less than 1 to approximately 80 [Pfahler et al., 1991]. A possible size effect was noted for the silicone oil experiments; namely, for a channel with  $3.0\text{-}\mu\text{m}$  depth,  $fRe$  did not remain constant as  $Re$  varied from 0.01 to 0.3.

In addition to measuring friction factors, Choi et al. (1991) measured surface roughness and heat transfer coefficients for nitrogen gas flowing through microtubes with diameters in the range of 3 to  $81 \mu\text{m}$  and  $L/D$  ratios of 640 to 8100. The measured friction factors in both the laminar and turbulent region were lower than predicted by macroscale theory. The measured absolute root mean square (rms) roughness was in the range of 10 to 80 nm, such that the normalized rms roughness,  $\epsilon/D$ , was less than 0.006 for all but one case. No variations were observed that appeared to depend on roughness.

A similar study of flows through microtubes with diameters of 19 to  $102 \mu\text{m}$  obtained extremely high Reynolds numbers for microscale conditions, up to 20,000 [Yu et al., 1995]. The normalized roughness of the tubes,  $\epsilon/D$ , was estimated at 0.0003. For both water and gas, the measured friction factors were lower than macroscale predictions, by approximately 19% in laminar flow and 5% in the turbulent flow regime.

To aid in comparing the results of these studies, a normalized friction factor,  $C^*$ , is defined as:

$$C^* = \frac{(fRe)_{\text{experimental}}}{(fRe)_{\text{theoretical}}} \quad (6.28)$$

The wide variability of results is illustrated in Figure 6.5. There is also wide variability in experimental conditions, microchannel geometries and methodology. However, the inconsistencies demonstrate the need for detailed velocity measurements in order to elucidate potential microscale effects and mechanisms in these channels.

### 6.2.1 Proposed Explanations for Measured Behavior

Thus far, the explanations offered in the literature for anomalous behavior of friction factor and flow resistance in microchannels include surface/roughness effects and electrical charge, variations in viscosity, microrotational effects of individual fluid molecules, "early" transition to turbulence, entrance effects and inaccuracies in measuring channel dimensions.

In macroscale theory, small to moderate surface roughness does not affect the flow resistance relationship in the laminar region [White, 1994]. Microscale results are inconclusive regarding the effects of surface roughness on resistance in the laminar region. Resistance results have shown both a strong increase due to roughness [Wu and Little, 1983] and no effect due to roughness [Choi et al., 1991].

In terms of surface effects on viscosity, a roughness viscosity model (RVM) has been introduced by Mala (1999), based on work by Merkle et al. (1974). Assuming that surface roughness increases the momentum transfer near the wall, Mala (1999) proposed that the roughness viscosity,  $\mu_r$ , as a function of  $r$ , is higher near the wall and proportional to the Reynolds number. Implementing this roughness-viscosity model for water flowing through trapezoidal channels, Qu et al. (2000) found reasonable agreement with model prediction and experimental results in most cases. However, the model did not

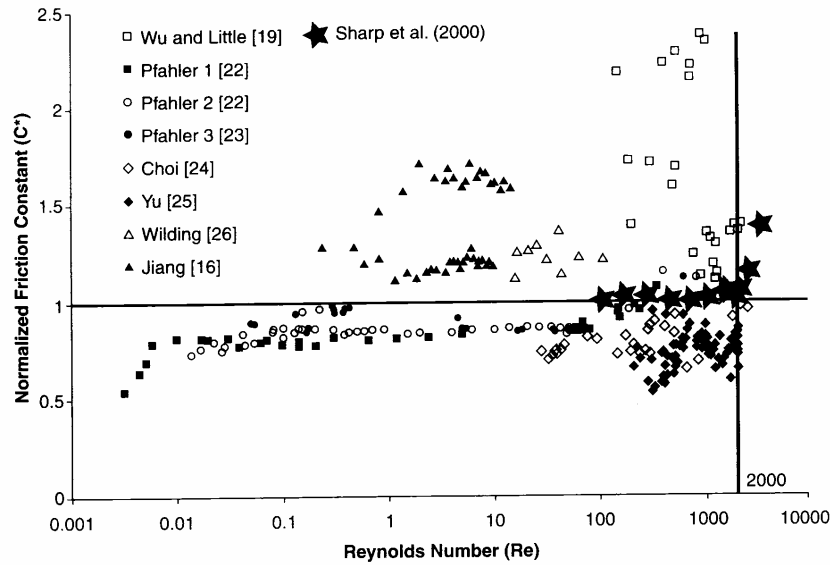


FIGURE 6.5 Comparison of  $C^*$  vs. Reynolds number for several previous studies. Data from Papautsky et al. (1999a), with additional data from Sharp et al. (2000). References are [19] Wu and Little (1983), [22] Pfahler et al. (1990a), [23] Pfahler et al. (1991), [24] Choi et al. (1991), [25] Yu et al. (1995), [26] Wilding et al. (1994) and [16] Jiang et al. (1995).

accurately depict the increased slope in the relationship between pressure drop and Reynolds number observed in the same experiments for  $Re \geq 500$ .

It is possible that unexpected electrokinetic effects occur at the interface between the channel and the fluid due to chemical interactions. These effects have not been adequately addressed to date in the flow resistance studies.

Direct measurement of viscosity in very thin layers, or thin films, has been performed by Israelachvili (1986). The viscosity of water was found to retain its bulk viscosity value to within 10% even in a film as thin as 5 nm. Concentrated and dilute NaCl/KCl solutions were also tested to assess the impact of double-layer forces on the value of viscosity near a surface. The viscosity of these solutions also remained only minimally affected until the last molecular layer near the wall. Based on these measurements, the viscosity of fluid in the wall region is not expected to vary significantly from the bulk value, even in the presence of possible charging effects, bringing the explanations of Mala and Li (1999) and Qu et al. (2000) into question.

As previously mentioned, it is possible that the very high shear rates in these microchannels cause normally Newtonian fluids to behave in a non-Newtonian fashion. The shear rates in Sharp et al. (2000) were as high as  $7.2 \times 10^5 \text{ s}^{-1}$ . Measuring the rheology of fluids at very high shear rates is challenging. Novotny and Eckert (1974), using a flat plate rheometer, determined that the relationship between shear stress and shear rate is still linear for water at a shear rate of  $10,000 \text{ s}^{-1}$ . The possibility that anomalous effects are caused by non-Newtonian behavior above shear rates of  $10^4 \text{ s}^{-1}$  needs to be explored.

A model based upon micropolar fluid theory has been implemented by Papautsky et al. (1999a) in order to interpret their experimental results (Reynolds numbers 1 to 20). Eringen (1964) first proposed this type of theory, which takes into account microvolume elements capable of independently translating, rotating and deforming. The equations for a "micropolar fluid" include additional terms accounting for the independent behavior of these elements. The equations have been solved numerically in Papautsky

et al. (1999a) for flow in rectangular channels. The model predicts an increase in flow resistance, in better agreement with their data than conventional predictions.

One explanation often offered to explain the increase of flow resistance in microchannels is that scaling considerations somehow trigger the transition to turbulence at a critical Reynolds number lower than the value of 1800 to 2000 commonly accepted in macroscale pipe flows. If the critical Reynolds number is lower, then disturbances introduced into the flow by unsteadiness in the flow source, sharp inlet conditions or any other source would begin to grow and eventually the flow would become fully turbulent. The majority of flow behavior studies thus far have relied upon bulk flow measurements and have not been able to quantitatively assess the spatial or temporal instabilities in the microflows. Thus, the evidence suggesting “early transition to turbulence” has been based solely on the trends in the resistance data (see, for example, the discussion of the experiment of Peng et al. [1994] presented previously). “Early transition to turbulence” has also been suggested as an explanation for anomalous behavior of the relationship between the pressure gradient,  $\Delta p/L$ , and  $Q$  by Mala and Li (1999), who reported a transition to turbulence at  $Re > 300$  to 900 and fully developed turbulent flows at  $Re \geq 1000$  to 1500.

In Sharp et al.’s (2000) resistance experiments, there is no evidence that transition to turbulence occurs for  $Re < 2000$ . The magnitude of spatial and temporal variations measured using micro-particle image velocimetry (PIV) is also inconsistent with a transition to turbulence for  $Re < 2000$ .

Certainly, the inclusion or exclusion of entrance effects could affect the magnitude of the measured friction factor. For example, the  $L/D$  ratio in Peng et al.’s (1994) experiments ranged from 145 to 376. The Reynolds number range was 50 to 4000. The entrance length can be approximated as  $L_e/D = 0.06 \times Re$  [White, 1994], which brings into question the validity of certain regions of the results. In particular, in certain experiments ( $D_h = 267 \mu\text{m}$ ) of Peng et al. (1994), the entrance length is estimated at half the length of the test section for the higher Reynolds number data by the above criterion.

Regardless of the geometry, it is extremely difficult to accurately measure the dimensions of these microchannels, particularly when one of the dimensions is on the order of a couple of microns. The pressure drop in a round capillary is inversely proportional to  $D^4$  (Eq. (21), where  $D = 2a$ ), so an inaccuracy of 5% in measuring  $D$  can bias resistance results by 20%, enough to explain the majority of the discrepancies between the conventional macroscopic resistance predictions and the observed values in Figure 6.5.

## 6.2.2 Measurements of Velocity in Microchannels

Along with the growth of research in microdevices, rapid development of experimental techniques for investigating flows in such devices is also underway, including modification of experimental techniques commonly applied at the macroscale and development of new techniques. Measurements of velocities in microchannels have been obtained using bulk flow, point-wise and field measurements. Each technique has certain advantages making it more suitable to provide a specific type of flowfield information.

The majority of flow resistance data to date has been obtained through the use of bulk flow measurements. This type of measurement generally includes a method for measuring flowrate, such as an in-line flowmeter, the timed collection of fluid at the outlet and pressure taps located at the inlet and outlet or simply at the inlet if the pressure at the outlet is known. Bulk flow measurements require no optical access to the microchannel, there are no restrictions on the geometrical parameters of the channel, and no seeding is required. However, given the disagreement in results regarding microscale effects on flow resistance in particular, bulk flow measurements are lacking in detail sufficient to discern potential mechanisms causing deviation from macroscale theory. Detailed measurements of flow velocity are also useful for optimizing the design of complex microdevices for mixing, separation, reaction and thermal control.

The first micro-PIV measurements were made by Santiago et al. (1998) in a Hele–Shaw cell. These velocity field measurements were resolved to  $6.9 \mu\text{m}$  in the lateral directions and  $1.5 \mu\text{m}$  in the depth direction and demonstrated the applicability of the well-established PIV technique for microflows. Micro-PIV measurements in a rectangular glass microchannel with 200-nm fluorescent tracer particles ( $Re < 1$ ) have been described in Meinhart et al. (1999). With improved acquisition and analysis, the lateral resolution was  $13.6 \mu\text{m}$  in the streamwise direction and significantly better,  $0.9 \mu\text{m}$ , in the cross-stream



direction, the direction of highest velocity variation. The first application of micro-PIV to a circular capillary was performed by Koutsiaris et al. (1999) in a 236- $\mu\text{m}$ -diameter channel with  $Re \ll 1$ . The seeding particles were 10- $\mu\text{m}$  glass spheres, and the resolution of the measurements was 26.2  $\mu\text{m}$  in the cross-stream direction. The measured velocity profiles agreed well with the predicted laminar parabolic profiles. More recently, micro-PIV has been used to study the velocity profiles and turbulence statistics of water flows in circular channels with  $D \sim 100$  to 250  $\mu\text{m}$  and  $Re$  up to 3000 by Sharp et al. (2000), using 2- $\mu\text{m}$  fluorescent particles.

Alternate visual methods applied to microchannel velocity measurements have been demonstrated by numerous researchers [Brody et al., 1996; Ovryn, 1999; Paul et al., 1998b; Taylor and Yeung, 1993; Webb and Maynes, 1999]. Molecular tagging velocimetry (MTV) was adapted to the microscale by Webb and Maynes (1999), where velocity profiles were obtained in circular tubes with  $D = 705 \mu\text{m}$  for  $Re = 800$  to 2200. The spatial resolution of these measurements was 2.1  $\mu\text{m}$ . The measured velocity profiles were consistent with macroscale laminar predictions for  $Re \leq 1600$ . A departure from laminar flow theory was noted at  $Re = 2168$ . Relevant development issues for microscale MTV are similar to those for PIV, namely, optical access and index of refraction compensation, particularly for curved surfaces, and optimized detection of the tracking particles (PIV) or beams (MTV).

Particle tracking, streak quantification or dye visualization can be relatively simple to implement given optical access and the ability to illuminate the flow. Care must be exercised in the extraction of quantitative data, particularly if the depth of field of the imaging device is large, if optical complications exist due to complex microchannel geometries, or if the particles or molecules are not accurately following the flow due to charge, size or density effects. Implementations of such techniques may be found in Taylor and Yeung (1993) and Brody et al. (1996).

Novel three-dimensional measurement techniques for microchannel flows are currently in development [Hitt and Lowe, 1999; Ovryn, 1999]. Building upon a technique already developed for the study of microscale structures, Hitt and Lowe (1999) used confocal imaging to build up a three-dimensional map of the "separation surface" following a bifurcation, where the "separation surface" describes the interfacial boundary between two components from different branches of the bifurcation. Using two laser scanning confocal microscopes, a series of thin (4.5 or 7.1  $\mu\text{m}$ ) horizontal slices were acquired and reconstruction software was used to combine these slices into a three-dimensional map. Again, optical access and effects are primary issues in the implementation of this method, and it is not suitable for unsteady flows. Ovryn (1999) sought to resolve and interpret the scattering pattern of a particle to determine its three-dimensional position, and he has applied this technique to laminar flow.

X-ray imaging techniques do not require optical access in the channel, though a contrast medium detectable by X-rays must be used as the working fluid. Lanzillotto et al. (1996) obtained flow displacement information from microradiograph images of emulsion flow through a 640- $\mu\text{m}$ -diameter tube and iododecane flow through a silicon V-groove chip.

The level of complexity increases when electrokinetic flows are considered. Paul et al. (1998b), Cummings et al. (1999) and Taylor and Yeung (1993) performed visual measurements in this environment. Paul et al. (1998b) seeded the flow with an uncaged fluorescent dye. Once the dye was uncaged by an initial ultraviolet (UV) laser pulse, the flow was illuminated by succeeding pulses of blue light for charge-coupled device (CCD) image acquisition, causing only the uncaged dye molecules to be excited. This technique was applied to both pressure-driven and electrokinetic flows in circular capillaries with diameters of the order 100  $\mu\text{m}$ . Since the dye transport represented both convection and diffusion, requisite care was necessary to separate the effects, as in Paul et al. (1998b). This method can also be used to acquire quantitative information regarding diffusion effects. Micro-PIV and nuclear magnetic resonance (NMR) techniques have also been applied to the measurement of velocities in electro-osmotic flow (Cummings et al., 1999; Manz et al., 1995).

Point-wise velocity measurements techniques have been applied at the microscale by Chen et al. (1997), Yazdanfar et al. (1997) and Tieu et al. (1995). Optical Doppler tomography, a point-wise measurement technique demonstrated by Chen et al. (1997), combines elements of Doppler velocimetry with optical coherence tomography in an effort to develop a system that can quantify the flow in biological tissues.

Chen et al. (1997) applied the technique to a 580- $\mu\text{m}$ -diameter conduit seeded with 1.7- $\mu\text{m}$  particles. An approximate parabolic profile was measured in the first test, and in the second it was shown that fluid particle velocities could be measured even with the conduit submerged in a highly scattering medium, as would be the case for particles in biological tissues. A similar measurement technique has been used for *in vivo* measurements in Yazdanfar et al. (1997). An adaptation of laser Doppler anemometry (LDA) techniques to microscale flows was demonstrated by Tieu et al. (1995), and point-wise data were obtained in a 175- $\mu\text{m}$  channel.

### 6.2.3 Nonlinear Channels

For practical MEMS applications, it is often useful to consider mixing or separation of components in microchannels. Numerous designs have been proposed, including T- and H-shaped channels, zigzag-shaped channels, two- and three-dimensional serpentine channels and multilaminators.

For example, Weigl and Yager (1999) have designed a T-sensor for implementation of assays in microchannels, as shown in Figure 6.6. A reference stream, a detection stream and a sample stream have been introduced through multiple T-junctions into a common channel. The design relied upon the differential diffusion of different-sized molecules to separate components in the sample stream. Differential diffusion rates are also fundamental to the design of the H-filter, used to separate components [Schulte et al., 2000]. Application of a slightly different T-channel design has been demonstrated for measurement of diffusion coefficients of a species in a complex fluid [Galambos and Forster, 1998].

A layering approach has been implemented by Branebjerg et al. (1996), splitting the streams and re-layering to increase interfacial area, thus promoting mixing. Adding complexity to the flowfield also has potential to increase the amount of mixing between streams, as demonstrated by Branebjerg et al.'s (1995) zigzag channel and the serpentine channels introduced by Liu et al. (2000). The three-dimensional serpentine channel in Liu et al. (2000) was designed to introduce chaotic advection into the system and further enhance mixing over a two-dimensional serpentine channel. A schematic of the three-dimensional serpentine channel is shown in Figure 6.7.

### 6.2.4 Capacitive Effects

While liquids are incompressible, the systems through which they flow may expand or contract in response to pressure in the liquid. This behavior can be described by analogy to flow in electrical circuits. In this analogy, fluid pressure corresponds to electrical voltage,  $p \sim V$ ; the volume flow rate corresponds to electrical current,  $Q \sim I$ ; and the flow resistance through a fluid element corresponds to an electrical resistor,  $R_{\text{flow}} \sim R_{\text{elec}}$ . Thus, for capillary flow,  $\Delta p = R_{\text{flow}}Q$ , where  $R_{\text{flow}} = 8\mu L/\pi a^4$  (cf. Eq. (21)), whereas in the electrical analogy  $\Delta V = R_{\text{elec}}I$ . If a fluid element is able to change its volume (expansion of plastic tubing, flexing in pressure transducer diaphragm, etc.), fluid continuity implies that:

$$\Delta Q = C_{\text{flow}} \frac{dp}{dt} \quad (6.29)$$

where  $C_{\text{flow}}$  is the capacitance of the fluid element. The corresponding electrical law is  $I = C_{\text{elec}} dV/dt$ , where  $C_{\text{elec}}$  is the electrical capacitance.

It is well known, in the context of electrical circuits, that a resistor and capacitor in combination cause transients whose time constant,  $\tau$ , is proportional to  $R_{\text{elec}}C_{\text{elec}}$ . In a microfluidic circuit, any capacitive element in combination with a flow resistance leads to analogous transients whose time constant is proportional to  $R_{\text{flow}}C_{\text{flow}}$ . Since  $R_{\text{flow}}$  can be very large in microchannels, the time constant can be surprisingly large (i.e.,  $10^3$  s). Consequently, capacitive effects can cause significant and inconveniently long transients.

## 6.3 Electrokinetics Background

The first demonstration of electrokinetic phenomena is attributed to F.F. Reuss, who demonstrated electro-osmotic flow through a sand column in a paper published in the *Proceedings of the Imperial Society*

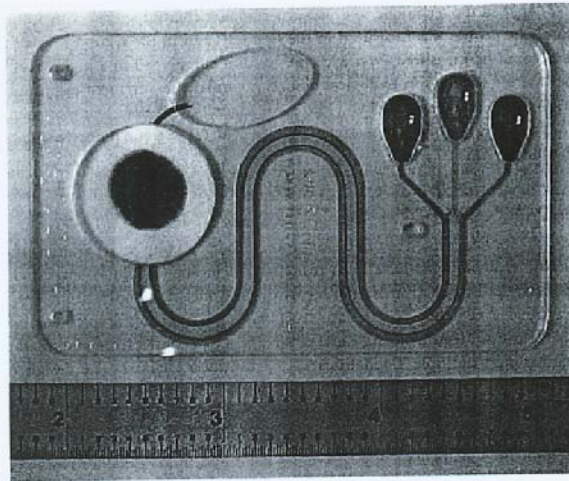


FIGURE 6.6 T-Sensor™ – Self-calibrating microchemical reactor and sensor. This design allows for self-calibration through the simultaneous flow of a reference solution on the opposite flank of the indicator stream from the sample to be analyzed. (Courtesy of Micronics, Inc., Redmond, WA.)

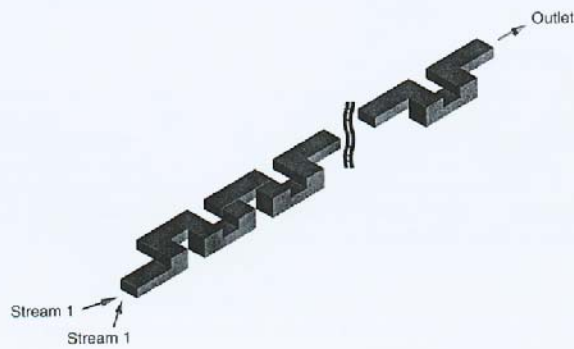


FIGURE 6.7 Three-dimensional serpentine channel. (From Liu, R.H., et al. (2000) *J. MEMS* 9, 190–197, ASME, New York. With permission.)

of *Naturalists of Moscow* in 1809 [Probstein, 1994]. In the latter part of the 20th century, the main applications of electrokinetic phenomena have been fairly wide ranging, from the dewatering of soils and waste sludges using electric fields [Hiemenz and Rajagopalan, 1997] to the study of the stability of colloidal suspensions for household paint to devices that use electrophoretic mass transfer of colloidal suspensions to produce images on a planar substrate [Kitahara and Watanabe, 1984]. A community that has paid particular attention to the study of mass and momentum transport using electrokinetic effects is the developers of capillary electrophoresis (CE) devices [Manz et al., 1994]. CE devices are used to

separate biological and chemical species by their electrophoretic mobility (roughly speaking, by their mass-to-charge ratio). These traditional CE systems incorporate on-line detection schemes such as ultra-violet radiation scatter/absorption and laser-induced fluorescence [Baker, 1995].

Electrokinetics is the general term describing phenomena that involve the interaction between solid surfaces, ionic solutions and macroscopic electric fields. Two important classes of electrokinetics are electrophoresis and electro-osmosis, where the motions of solid bodies and fluids, respectively, occur when an external electric field is applied to the system. Electrophoresis is the induced motion of colloidal particles or molecules suspended in liquids that results from the application of an electric field. Electro-osmosis describes the motion of electrolyte liquids with respect to a fixed solid that results when an electric field is applied parallel to the surface. An example of electro-osmosis is the fluid pumping that occurs in a microcapillary when an electric field is applied along the axis of the capillary [Probstein, 1994]. Two other phenomena also classified under electrokinetics are flows with a finite streaming potential and sedimentation potential. These phenomena are counter-examples of electro-osmosis and electrophoresis, respectively. Streaming potential is the spontaneous generation of an electric potential from a pressure-driven flow in a charged microchannel [Hunter, 1981; Scales et al., 1992]. Sedimentation potential is the generation of an electric potential that results from the sedimentation (e.g., due to gravity) of a charged particle [Russel et al., 1999]. All of the phenomena classified under the term electrokinetics are manifestations of the electrostatic component of the Lorentz force (on ions and surface charges) and Newton's second law of motion. These interactions between charged particles and electric fields often involve electric double layers formed at liquid/solid interfaces and an introduction to this phenomenon is presented below.

### 6.3.1 Electrical Double Layers

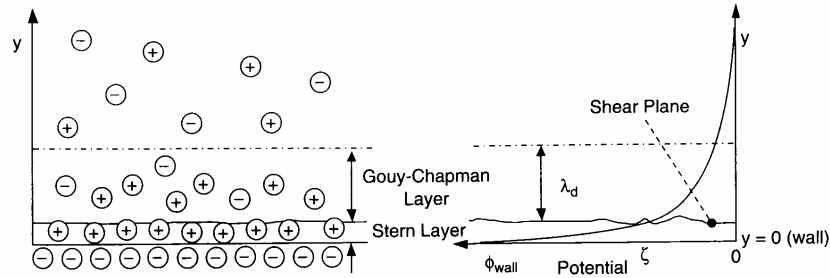
Most solid surfaces acquire a surface electric charge when brought into contact with an electrolyte (liquid). Mechanisms for the spontaneous charging of surface layers include the differential adsorption of ions from an electrolyte onto solid surfaces (e.g., ionic surfactants), the differential solution of ions from the surface to the electrolyte, and the deprotonation/ionization of surface groups [Hunter, 1981]. The most common of these in microfluidic electrokinetic systems is the deprotonation of surface groups on the surface of materials such as silica, glass, acrylic and polyester. In the case of glass and silica, the deprotonation of surface silanol groups (SiOH) determines the generated surface charge density. The magnitude of the net surface charge density at the liquid–solid interface is a function of the local pH. The equilibrium reaction associated with this deprotonation can be represented as:



Models describing this reaction have been proposed for several types of glass and silica [Hayes et al., 1993; Huang et al., 1993; Scales et al., 1992]. In practice, the full deprotonation of the glass surface, and therefore the maximum electro-osmotic flow mobility, is achieved for pH values greater than about 9.

In response to the surface charge generated at a liquid–solid interface, nearby ions of opposite charge in the electrolyte are attracted by the electric field produced by the surface charge, and ions of like charge are repelled. The spontaneously formed surface charge therefore forms a region near the surface called an electrical double layer (EDL) that supports a net excess of mobile ions with a polarity opposite to that of the wall. Figure 6.8 shows a schematic of the EDL for a negatively charged wall (e.g., as in the case of a glass surface). The region of excess charge formed by the counterions shielding the electric field of the wall can be used to impart a force (through ion drag) on the bulk fluid.

As shown in Figure 6.8, counterions reside in two regions divided into the Stern and Gouy–Chapman diffuse layers [Adamson and Gast, 1997]. The Stern layer counterions are adsorbed onto the wall, while the ions of the Gouy–Chapman diffuse layer are free to diffuse into the bulk fluid and therefore are available to impart work on the fluid. The plane separating the Stern and Gouy–Chapman layers is called the *shear plane*. The bulk liquid far from the wall is assumed to have net neutral charge. Also shown in Figure 6.8 is a sketch of the potential associated with the EDL. The magnitude of this potential is a maximum at the wall and drops rapidly through the Stern layer. The potential at the shear plane, which is also the



**FIGURE 6.8** Schematic of the electrical double layer (EDL): (Left) Distribution of co- and counterions near a charged wall. The Stern and Gouy–Chapman layers are shown with the Gouy–Chapman thickness roughly approximated as the Debye length of the solution. (Right) A plot of the negative potential distribution near a glass wall indicating the zeta potential, wall potential and location of the shear plane.

boundary of the fluid flow problem, is called the *zeta potential*,  $\zeta$ . Because of the difficulties associated with predicting the properties of the Stern layer [Hunter, 1981], the zeta potential is typically determined empirically from electro-osmotic or streaming potential flow measurements.

The simple treatment of the physics of the diffuse portion of the EDL presented here assumes a liquid with constant properties (i.e., constant viscosity and electrical permittivity). A more detailed model of the diffuse portion of the electrical double layer should include noncontinuum effects such as finite ion size effects and gradients in the dielectric strength and viscosity of the fluid [Hunter, 1981]. The width of the diffuse portion of the EDL is determined by the opposing forces of electrostatic attraction and thermal diffusion. This balance between electromigration and diffusive fluxes, together with the Nernst–Einstein equation relating ion diffusivity and mobility [Hiemenz and Rajagopalan, 1997], can be used to show that the concentration profile is described by the Boltzmann distribution. For an EDL on a flat plate, the Boltzmann distribution of ions of species  $i$ ,  $c_i$ , is

$$c_i(y) = c_{\infty,i} \exp\left(-\frac{ze\phi(y)}{kT}\right) \quad (6.31)$$

where  $c_{\infty,i}$  is the molar concentration of ion  $i$  in the bulk,  $z$  is the valance number of the ion,  $\phi$  is the local potential,  $T$  is temperature,  $e$  is the charge of an electron and  $k$  is Boltzmann's constant. The coordinate  $y$  is perpendicular to the wall, and the origin is at the shear plane of the EDL. The net charge density in the EDL,  $\rho_E$ , is related to the molar concentrations of  $N$  species using the relation:

$$\rho_E = F \sum_{i=1}^N z_i c_i \quad (6.32)$$

where  $F$  is Faraday's constant. The net charge density can also be related to the local potential in the diffuse EDL by the Poisson equation:

$$\nabla^2 \phi = \frac{-\rho_E}{\epsilon} \quad (6.33)$$

where  $\epsilon$  is the permittivity of the liquid. Substituting Eqs. (6.31) and (6.32) into Eq. (6.33), we find that:

$$\frac{d^2 \phi}{dy^2} = \frac{-F}{\epsilon} \sum_{i=1}^N z_i c_{\infty,i} \exp\left(-\frac{ze\phi(y)}{kT}\right) \quad (6.34)$$

For the simple case of a symmetric electrolyte with (two) monovalent ions, this relation becomes:

$$\frac{d^2\phi}{dy^2} = \frac{2Fz_1c_\infty}{\epsilon} \sinh\left(\frac{ze\phi(y)}{kT}\right) \quad (6.35)$$

where  $c_\infty$  is the molar concentration of each of the two ion species in the bulk. This relation is the nonlinear Poisson–Boltzmann equation. A closed form, analytical solution of this equation for the EDL on a flat wall is given by Adamson and Gast (1997).

A well-known approximation to the Poisson–Boltzmann solution, known as the Debye–Hückle limit, is to consider the case where the potential energy of ions in the EDL is small compared to their thermal energy so that the argument of the hyperbolic sine function in Eq. (6.35) is small. Applying this approximation, Eq. (6.35) becomes:

$$\frac{d^2\phi}{dy^2} = \frac{\phi(y)}{\lambda_D^2} \quad (6.36)$$

where  $\lambda_D$  is the Debye length of the electrolyte defined as:

$$\lambda_D \equiv \left(\frac{\epsilon kT}{2z^2 F^2 c_\infty}\right)^{\frac{1}{2}} \quad (6.37)$$

for a symmetric, monovalent electrolyte. The Debye length describes the characteristic thickness of the EDL which varies inversely with the square root of ion molar concentration. At typical biochemical, singly ionized buffer concentrations of 10 mM, the thickness of the EDL is therefore on the order of a few nanometers [Hiemenz and Rajagopalan, 1997]. In analyzing electrokinetic flow in microchannels, the Debye length should be compared to the characteristic dimension of the microchannel in order to classify the pertinent flow regime. Overbeek (1952a) points out that the Debye–Hückle approximation of the potential of the EDL holds remarkably well for values of the ratio  $ze\phi/(kT)$  up to approximately 2. This value is equivalent to a zeta potential of about 50 mV which is within the typical range of microfluidic applications.

Models of the physics of the EDLs can be used to extrapolate the zeta potential of particles and microchannels across a significant range of buffer concentration, fluid viscosity, electrical permittivity of electrolytes, and field strengths given only a few measurements. One of the most difficult zeta potential extrapolations to make is across different values of pH, as pH changes the equilibrium reactions associated with the charge at the liquid/solid interface.

A full formulation of the coupled system of equations describing electro-osmotic and electrokinetic flow includes the convective diffusion equations for each of the charged species in the system, the Poisson equation for both the applied electric field and the potential of the EDL and the equations of fluid motion. A few solutions to this transport problem relevant to microfluidic systems are presented below.

### 6.3.2 EOF with Finite EDL

Electro-osmotic flow (EOF) results when an electric field is applied through a liquid-filled microchannel having an EDL at the channel surfaces, as described above. This applied electric field introduces an electrostatic Lorentz body force:

$$\rho \mathbf{b} = \rho_e \mathbf{E} \quad (6.38)$$

into the equation of motion for the fluid, Eq. (6.3). Within the EDL, the electric field exerts a net force on the liquid, causing the fluid near the walls to move. Alternatively, one can describe the effect as simply the ion drag on the fluid associated with the electrophoresis of the ions in the EDL. The fluid in the EDL exerts a viscous force on the rest of the (net zero charge) liquid in the bulk of the channel. For EDLs

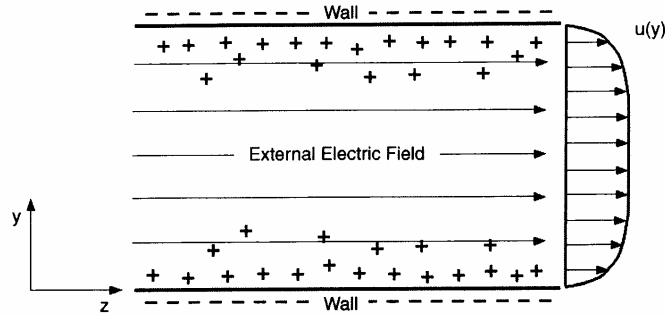


FIGURE 6.9 Schematic of an electro-osmotic flow channel with a finite EDL. The charges drawn in the figure indicate net charge. The boundary layers on either wall have a thickness on the order the Debye length of the solution. For nonoverlapping EDLs, the region near the center of the channel is net neutral.

much smaller than the channel dimension  $D$ , the fluid velocity reaches steady state in a short time  $t$  that is on the order of  $D^2/\nu$ , where  $\nu$  is the kinematic viscosity of the fluid. The resulting bulk electro-osmotic flow is depicted schematically in Figure 6.9.

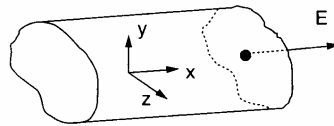


FIGURE 6.10 Illustration of a section of a long, straight channel having an arbitrary cross section.

The equation of motion for steady, low Reynolds number flow in the microchannel is given by:

$$\nabla p = \mu \nabla^2 \mathbf{u} + \rho_e \mathbf{E} \quad (6.39)$$

Substituting Eq. (6.33) for the charge density results in:

$$\nabla^2 \left( \mathbf{u} - \frac{\epsilon \mathbf{E}}{\mu} \phi \right) = \frac{\nabla p}{\mu} \quad (6.40)$$

In Eq. (6.40), the electric field,  $\mathbf{E}$ , can be brought into the Laplace operator because  $\nabla \cdot \mathbf{E} = \nabla \times \mathbf{E} = 0$ . Equation (6.40) is linear so the velocities caused by the pressure gradient and the electric field can be considered separately and then superposed as follows:

$$\nabla^2 \left( \mathbf{u}_{\text{EOF}} - \frac{\epsilon \mathbf{E}}{\mu} \phi \right) = 0 \quad (6.41)$$

$$\nabla^2 \mathbf{u}_{\text{pressure}} = \frac{\nabla p}{\mu} \quad (6.42)$$

Together with Eq. (6.2), these are the general equations for electro-osmotic flow in a microchannel. Evaluation of the pressure-driven flow component of velocity in a microchannel can leverage analytical solutions available for channels of various cross sections [White, 1991]. The pressure gradient can be

applied externally or may arise internally because of variations in the zeta-potential at the channel walls [Herr et al., 2000].

Now consider electro-osmosis in a long, straight microchannel with a finite width electrical double layer and an arbitrary cross section that remains constant along the flow direction ( $x$ -axis), as shown in Figure 6.10. The applied electric field is assumed to be uniform and along the  $x$ -axis of the microchannel. For the case where the potential at the wall is uniform, the solution to Eq. (6.41) is

$$u_{\text{EOF}} - \frac{\varepsilon E \zeta}{\mu} \phi = \frac{-\varepsilon E \zeta}{\mu} \quad (6.43)$$

with the zeta potential,  $\zeta$ , being the value of  $\phi$  at the top of the double layer. In Eq. (6.43),  $u_{\text{EOF}}$  and  $E$  are the unidirectional velocity and unidirectional applied electric field, respectively. The general expression for the electro-osmotic velocity, implicit in the potential, is then

$$u_{\text{EOF}}(y, z) = \frac{-\varepsilon E \zeta}{\mu} \left( 1 - \frac{\phi(y, z)}{\zeta} \right) \quad (6.44)$$

To compute values for the velocity given in Eq. (6.44), an expression for the potential  $\phi(y, z)$  is required. In general,  $\phi(y, z)$  can be computed numerically from Eq. (6.34), but analytical solutions exist for several geometries. Using the Boltzmann equation for a symmetric analyte and the Debye–Hückel approximation discussed in the previous section, Rice and Whitehead (1965) give the solution for electro-osmosis in a long cylindrical capillary:

$$u_{\text{EOF}}(r) = \frac{-\varepsilon E \zeta}{\mu} \left( 1 - \frac{I_0(r/\lambda_D)}{I_0(r/a)} \right) \quad (6.45)$$

In Eq. (6.45),  $I_0$  is the zero-order modified Bessel function of the first kind,  $r$  is the radial direction and  $a$  is the radius of the cylindrical capillary. This solution can be superposed with the solution of Eq. (6.42) for a constant pressure gradient. The resulting composite solution is

$$u(r) = \frac{-\varepsilon E \zeta}{\mu} \left( 1 - \frac{I_0(r/\lambda_D)}{I_0(r/a)} \right) - \frac{dp}{dx} \frac{a^2}{4\mu} \left( 1 - \frac{r^2}{a^2} \right) \quad (6.46)$$

Burgeon and Nakache (1964) give a solution for electro-osmotic flow between two long, parallel plates for a finite EDL thickness. For other more complex geometries and many unsteady problems, numerical solutions for the electro-osmotic flow are required. However, when the Debye length is finite, but much smaller than other dimensions (e.g., the width of the microchannel), the disparate length scales can make numerical solutions difficult [Bianchi et al., 2000; Patankar and Hu, 1998]. In many cases, EOF in complex geometries can be determined numerically using a thin double-layer assumption described in the next section.

### 6.3.3 Thin EDL Electro-Osmotic Flow

This section presents a brief analysis of electro-osmotic flow in microchannels with thin EDLs. Figure 6.11 shows a schematic of an electro-osmotic flow in a microchannel with zero pressure gradient. As shown in the figure, the Debye length of typical electrolytes used in microfabricated electrokinetic systems is much smaller than the hydraulic diameter of the channels. Typical ratios of Debye length-to-channel diameter are less than  $10^{-4}$ . For low Reynolds number, electro-osmotic flow in a cylindrical channel in the presence of a constant axial pressure gradient and a Debye length much smaller than the capillary radius, the solution of the velocity field is simply:

$$u(r) = \frac{\varepsilon \zeta E}{\mu} \frac{dp}{dx} \frac{(a^2 - r^2)}{4\mu} \quad (6.47)$$



- Electric double-layers thin compared to channel dimension
- Electrically insulating channel walls
- Low Reynolds number
- Low product of Reynolds and Strouhal numbers
- Parallel flow at inlets and outlets
- Uniform fluid properties

When these conditions are met, the electro-osmotic streamlines exactly correspond to the electric field-lines. The approximation is applicable to systems with a microchannel length scale less than 100  $\mu\text{m}$ , a Debye length less than 10 nm, a velocity scale less than 1 mm/s and a characteristic forcing function time scale greater than 10 ms [Santiago, 2001]. An important part of this similarity proof is to show the applicability of the Helmholtz–Smolouchowski equation in describing the local velocity field at the slip surface that bounds the “internal” flow of the microchannel which excludes the EDL. The Helmholtz–Smolouchowski equation can be shown to hold for most microfluidic systems where the motion of the EDL is dominated by the Lorentz and viscous forces. In such systems, we can consider the velocity field of the fluid outside of the EDL as a three-dimensional, unsteady flow of a viscous fluid of zero net charge that is bounded by the following slip velocity condition:

$$u_{\text{slip}} = -\frac{\epsilon\zeta}{\mu} E_{\text{slip}} \quad (6.50)$$

where the subscript “slip” indicates a quantity evaluated at the slip surface at the top of the EDL (in practice, a few Debye lengths from the wall). The velocity along this slip surface is, for thin EDLs, similar to the electric field. This equation and the condition of similarity also hold for inlets and outlets of the flow domain which have zero imposed pressure gradients.

The complete velocity field of the flow bounded by the slip surface (and inlets and outlets) can be shown to be similar to the electric field [Santiago, 2001]. We nondimensionalize the Navier–Stokes equations by a characteristic velocity and length scale  $U_s$  and  $L_s$ , respectively. The pressure  $p$  is nondimensionalized by the viscous pressure  $\mu U_s/L_s$ . The Reynolds and Strouhal numbers are  $Re = \rho L_s U_s/\mu$  and  $St = L_s/\tau U_s$ , respectively, where  $\tau$  is the characteristic time scale of a forcing function. The equation of motion is

$$Re St \frac{\partial \mathbf{u}'}{\partial t'} + (Re \mathbf{u}' \cdot \nabla \mathbf{u}') = -\nabla p' + \nabla^2 \mathbf{u}' \quad (6.51)$$

Note that the right-most term in Eq. (6.51) can be expanded using a well-known vector identity:

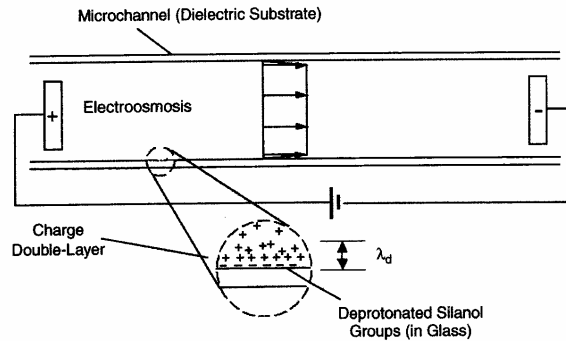
$$\nabla^2 \mathbf{u}' = \nabla(\nabla \cdot \mathbf{u}') - \nabla \times \nabla \times \mathbf{u}' \quad (6.52)$$

We can now propose a solution to Eq. (6.52) that is proportional to the electric field and of the form:

$$\mathbf{u}' = \frac{c_o}{U} \mathbf{E} \quad (6.53)$$

where  $c_o$  is a proportionality constant and  $\mathbf{E}$  is the electric field driving the fluid. Because we have assumed that the EDL is thin, the electric field at the slip surface can be approximated by the electric field at the wall. The electric field bounded by the slip surface satisfies Faraday’s and Gauss’ laws:

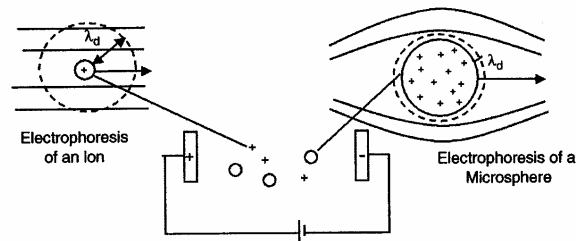
$$\nabla \cdot \mathbf{E} = \nabla \times \mathbf{E} = 0 \quad (6.54)$$



**FIGURE 6.11** Schematic of electro-osmotic flow in a glass microchannel with a thin EDL. A zero pressure gradient “plug flow” is shown. The electrodes on the ends of the channel indicate the polarity of the electric field.

This equation can be derived by evaluating Eq. (6.46) in the limit of a thin EDL (i.e., a small value of  $\lambda_D/a$ ).

The zeta potential typically determines flow velocities and flow rates in common thin EDL systems. As mentioned above, this quantity can often be interpreted as an empirically measured mobility parameter that determines the local velocity of the flow at the top of the electrical double layer.



**FIGURE 6.12** Two limiting limits of electrophoresis in an electrolyte. Shown are electrophoretic particles in the electric field generated between two electrodes. On the left is the detail of a charged ion with a characteristic dimension much smaller than the Debye length of the electrolyte. On the right is a charged microsphere with a diameter much larger than the Debye length.

can be approximately related to the local surface charge density on the wall and the bulk fluid properties by applying continuum field and flow theory. Theoretically, the zeta potential is defined as the value of the electrostatic potential at the plane that separates double-layer counterions that are mobile from those that are fixed. For the case of zero applied pressure gradients, Eq. (6.47) reduces to the well-known Helmholtz–Smolouchowski relation for electro-osmotic flow:  $u = \epsilon\zeta E/\mu$  [Probstein, 1994].

### 6.3.4 Electrophoresis

Many electrokinetic microfluidic systems leverage the combination of electro-osmotic and electrophoresis to achieve biological separations and to transport charged particles (e.g., biological assay microbeads)

and ions. Because of this, we present here a short introduction to electrophoresis. Electrophoresis is the induced motion of colloidal particles or molecules suspended in polar solutions that results from application of an electric field. Two important regimes of electrophoresis depicted in Figure 6.12 are for the electromigration of species that are either large or small compared to the Debye length of the ionic solution in which they are suspended.

Electrophoresis of ionic molecules and macromolecules can be described as a simple balance between the electrostatic force on the molecule and the viscous drag associated with its resulting motion. As a result, the electrophoretic mobility (velocity-to-electric-field ratio) of molecules is a function of the size/molecular weight of the molecule and directly proportional to their valence number, or

$$u = \frac{qE}{3\pi\mu d} \quad (d \ll \lambda_d) \quad (6.48)$$

where  $q$  is the total molecule charge and  $d$  is the Stokes diameter of the particle (the diameter of a sphere of equal drag). In comparison, the electrophoresis of relatively large solid particles, such as 100- to 10,000-nm-diameter polystyrene spheres and single-celled organisms is a function of the electrostatic forces on the surface charge, the electrostatic forces on their charge double layers, and the viscous drag associated with both the motion of the body and the motion of the ionic cloud. For a wide range of cases where the ratio of particle diameter to Debye length is large so that, locally, the ionic cloud near the particle surface can be approximated by the EDL relations for a flat plate, the velocity of an electrophoretic particle reduces simply to:

$$u = \frac{\epsilon\zeta E}{\mu} \quad (d \gg \lambda_d) \quad (6.49)$$

where the dimension  $d$  in the inequality condition is a characteristic dimension of the particle (e.g., its Stokes diameter). This equation was shown by Smoluchowski (1903) to be independent of particle shape. The reader will note that this, again, is the Helmholtz–Smoluchowski equation introduced earlier (with a change of sign).

The two expressions above describing the electrophoresis of particles can be expressed in terms of a mobility  $v_{\text{eph}}$  equal to  $q/(3\pi\mu d)$  and  $\epsilon\zeta/\mu$  for characteristic particle dimensions much smaller and much larger than the Debye length, respectively. Note also that for the simple case of a fluid with uniform properties, the solution of the drift velocity of electrophoretic particles with respect to the bulk liquid are similar (i.e., parallel and directly proportional) to lines of electric field.

Several solutions of the particle velocity and velocity field in the region of an electrophoretic particle with a finite EDL exist [Hunter, 1981; Russel et al., 1999]. A well-known solution is that of Henry (1948) for the flow around an electrophoretic sphere in the Debye–Huckel limit. The  $d \gg \lambda_d$  limit of Henry's solution results in Eq. (6.49).

### 6.3.5 Similarity between Electric and Velocity Fields for Electro-Osmosis and Electrophoresis

The previous sections have described the solution for electro-osmotic velocity field in straight, uniform cross-section channels. In general, solving for the electro-osmotic velocity field in more complex geometries requires a solution of the electric field and charge density in the microchannel, together with a solution to the Navier–Stokes equations. For simple electro-osmotic flows, however, Overbeek (1952b) has argued that the fluid velocity is parallel to the electric field everywhere. This concept has also been discussed by Cummings et al. (2000) and Santiago (2001). A set of sufficient conditions for which there exists a velocity field solution that is similar to the electric field is

- Uniform zeta potential

Substituting Eqs. (6.53) and (6.54) into Eq. (6.51) yields:

$$ReSt \frac{\partial \mathbf{u}'}{\partial t'} + Re(\mathbf{u}' \cdot \nabla \mathbf{u}') = -\nabla p' \quad (6.55)$$

This is the condition that must hold for Eq. (6.53) to be a solution to Eq. (6.51). One limiting case where this holds is for very high Reynolds number flows where inertial and pressure forces are much larger than viscous forces. Such flows are not applicable to microfluidics. Another limiting case applicable here is when  $Re$  and  $ReSt$  are both small, so that the condition for Eq. (6.53) to hold becomes:

$$\nabla p' = 0 \quad (6.56)$$

Therefore, we see that for small  $Re$  and  $ReSt$  and the pressure gradient at the inlets and outlets equal to zero, Eq. (6.53) is a valid solution to the flow bounded by the slip surface, inlets and outlets (note that these arguments do not show the uniqueness of this solution). We can now consider the boundary conditions required to determine the value of the proportionality constant  $c_o$ . Setting Eq. (6.50) equal to Eq. (6.53) we see that  $c_o = \epsilon\zeta/\eta$ , so that if the simple flow conditions are met, then the velocity everywhere in the fluid bounded by the slip surface is given by:

$$\mathbf{u}(x, y, z, t) = -\frac{\epsilon\zeta}{\mu} \mathbf{E}(x, y, z, t) \quad (6.57)$$

Equation (6.57) is the Helmholtz–Smoluchowski equation shown to be a valid solution to the quasi-steady velocity field in electro-osmotic flow with  $\zeta$  the value of the zeta potential at the slip surface. This result greatly simplifies the modeling of simple electro-osmotic flows, as simple Laplace equation solvers can be used to solve for the electric potential and then, using Eq. (6.57), for the velocity field. This approach has been applied to the optimization of microchannel geometries and verified experimentally [Molho et al., 2000]. Figure 6.13 shows the superposition of particle pathlines/streamlines and predicted electric fieldlines [Devasenathipathy and Santiago, 2000] in a steady flow that meets the simple electro-osmotic flow conditions summarized above. As shown in the figure, the electro-osmotic flow field streamlines are very well approximated by electric fieldlines.

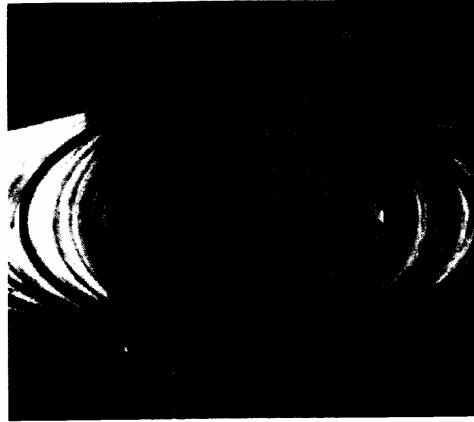
Note that for the simple electro-osmotic flow conditions analyzed here, the electrophoretic drift velocities (with respect to the bulk fluid) are also similar to the electric field, as mentioned above. Therefore, the time-averaged, total (drift plus fluid) velocity field of electrophoretic particles can be shown to be

$$\mathbf{u}_{\text{particle}} = \left( v_{\text{eph}} - \frac{\epsilon\zeta}{\mu} \right) \mathbf{E} \quad (6.58)$$

Here, we use the electrophoretic mobility  $v_{\text{eph}}$  that was defined earlier and  $-\epsilon\zeta/\mu$  is the electro-osmotic flow mobility of the microchannel walls.

### 6.3.6 Electrokinetic Microchips

The advent of microfabrication and microelectromechanical systems (MEMS) technology has seen an application of electrokinetics as a method for pumping fluids on microchips [Jacobson et al., 1994; Manz et al., 1994]. On-chip electro-osmotic pumping is easily incorporated into electrophoretic and chromatographic separations and these “laboratories on a chip” offer distinct advantages over the traditional, free-standing capillary systems. Advantages include reduced reagent use, tight control of geometry, the ability to network and control multiple channels on a chip, the possibility of massively parallel analytical

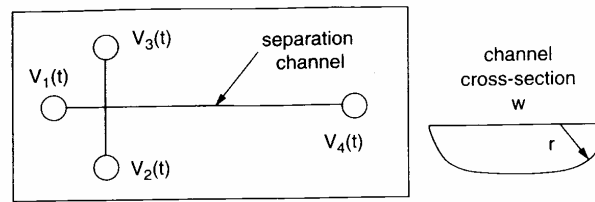


**FIGURE 6.13** Comparison between experimentally determined electrokinetic particle pathlines at a microchannel intersection and predicted electric field lines. The light streaks show the path lines of 0- to 5- $\mu\text{m}$ -diameter particles advecting through an intersection of two microchannels. The electrophoretic drift velocities and electro-osmotic flow velocities of the particles are approximately equal. The channels have a trapezoidal cross section having a hydraulic diameter of 18  $\mu\text{m}$  (130  $\mu\text{m}$  wide at the top, 60  $\mu\text{m}$  wide at the base and 50  $\mu\text{m}$  deep). The superposed, heavy black lines correspond to a prediction of electric field lines in the same geometry. The predicted electric field lines very closely approximate the experimentally determined pathlines of the flow. (From Devasenathipathy, S. and Santiago, J.G., unpublished results, Stanford University, Stanford, CA. With permission.)

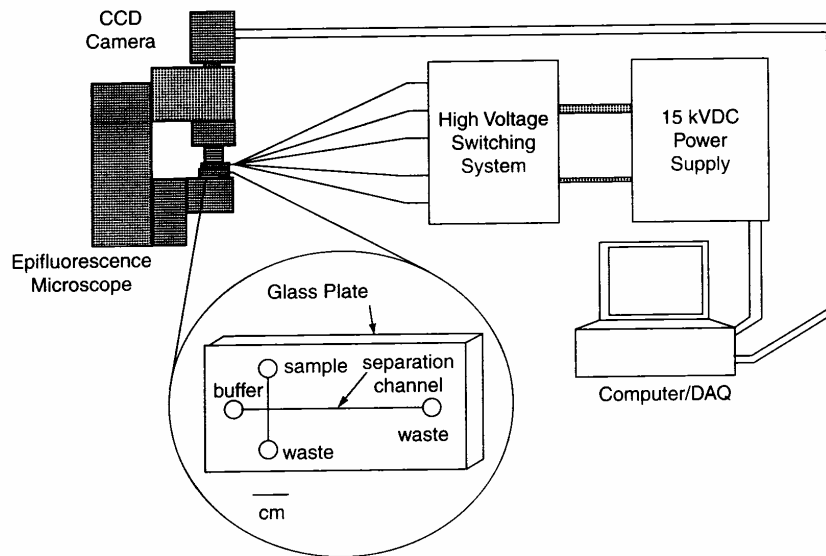
process on a single chip, the use of chip substrate as a heat sink (for high field separations) and the many advantages that follow the realization of a portable device [Khaledi, 1998]. Electrokinetic effects significantly extend the current design space of microsystems technology by offering unique methods of sample handling, mixing, separation and detection of biological species including cells, microparticles and molecules.

This section presents typical characteristics of a microchannel network fabricated using microlithographic techniques (see description of fabrication in the next section). Figure 6.14 shows a top view schematic of a typical microchannel fluidic chip used for capillary electrophoresis [Manz et al., 1994]. In this simple example, the channels are etched on a dielectric substrate and bonded to a plate (coverslip) of the same material. The circles in the schematic represent liquid reservoirs that connect with the channels through holes drilled through the coverslip. The parameters  $V_1$  through  $V_4$  are time-dependent voltages applied at each reservoir "well." A typical voltage switching system may apply voltages with on/off ramp profiles of approximately 10,000 V/s or less so that the flow can often be approximated as quasi-steady.

The four-well system shown in Figure 6.14 can be used to perform an electrophoretic separation by injecting a sample from well #3 to well #2 by applying a potential difference between these wells. During this injection phase, the sample is confined or "pinched" to a small region within the separation channel by flowing solution from well #1 to #2 and from well #4 to well #2. The amount of desirable pinching is generally a trade-off between separation efficiency and sensitivity. Alarie et al. (2000) have found that the pinching was optimized (implying a minimization of the injected sample plug) when the flow rate of sample from well #3 was 44% of the total amount of flow entering the intersection. Next, the injection phase potential is deactivated and a potential is applied between well #1 and well #4 to dispense the injection plug into the separation channel and begin the electrophoretic separation. The potential between wells #1 and #2 is referred to as the *separation potential*. During the separation phase, potentials are applied at wells #2 and #3 which "retract" or "pull back" the solution-filled streams on either side of the separation channel. As with the pinching described above, the amount of "pull back" is a trade-off between



**FIGURE 6.14** Schematic of a typical electrokinetic microchannel chip.  $V_1$  through  $V_5$  represent time-dependent voltages applied to each microchannel. The channel cross section shown is for the [common case] of an isotropically etched glass substrate with a mask line width of  $(w - 2r)$ .

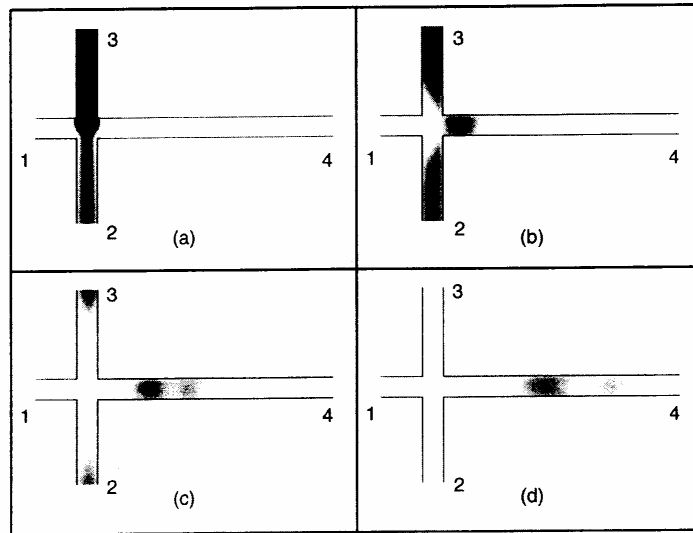


**FIGURE 6.15** Schematic of microfabricated capillary electrophoresis system, flow imaging system, high voltage control box and data acquisition computer.

separation efficiency and sensitivity. Alarie et al. (2000) have found that dispensing the sample plug into the separation channel was optimized when the flow rate of sample toward well #4 was 48% of the total amount of flow entering the intersection.

Figure 6.15 shows a schematic of a system that was used to perform and image an electrophoretic separation in a microfluidic chip. The microchip depicted schematically in Figure 6.15 is commercially available from Micralyne, Inc., Alberta, Canada. The width and depth of the channels are 50 and 20  $\mu\text{m}$ , respectively. The separation channel is 80 mm from the intersection to the waste well (well #4 in Figure 6.14). A high-voltage switching system allows for rapid switching between the injection and separation voltages and a computer, epifluorescent microscope and CCD camera are used to image the electrophoretic separation. The system depicted in Figure 6.15 is used to design and characterize electrokinetic injections; in a typical electrophoresis application, the CCD camera would be replaced with a point detector (e.g., a photomultiplier tube) near well #4.

Figure 6.16 shows an injection and separation sequence of 200  $\mu\text{M}$  solutions of fluorescein and Bodipy dyes (Molecular Probes, Inc., Eugene, OR). Images (a) through (d) are each 20-ms exposures separated by 250 ms. In Figure 6.16a, the sample is injected applying 0.5 kV and ground to well #3 and well #2, respectively. The sample volume at the intersection is “pinched” by flowing buffer from well #1 and well #4. Once a



**FIGURE 6.16** Separation sequence of Bodipy and fluorescein in a microfabricated capillary electrophoresis system. The channels shown are 50  $\mu\text{m}$  wide and 20  $\mu\text{m}$  deep. The fluorescence images are 20-ms exposures, and consecutive images are separated by 250 ms. A background image has been subtracted from each of the images, and the channel walls were drawn in for clarity. (From Bharadwaj, R., and Santiago, J.G., unpublished results, Stanford University, Stanford, CA. With permission.)

steady flow condition is achieved, the voltages are switched to inject a small sample plug into the separation channel. During this separation phase, the voltages applied at well #1 and well #4 are 2.4 kV and ground, respectively. The sample remaining in the injection channel is “retracted” from the intersection by applying 1.4 kV to both well #2 and well #3. During the separation, the electric field strength in the separation channel is about 200 V/cm. The electrokinetic injection introduces an approximately 400-pL volume of the homogenous sample mixture into the separation channel, as seen in Figure 6.16b. The Bodipy dye is neutral so its species velocity is identical to that of the electro-osmotic flow velocity. The relatively high electro-osmotic flow velocity in the capillary carries both the neutral Bodipy and negatively charged fluorescein toward well #4. The negative electrophoretic mobility of the fluorescein moves it against the electro-osmotic bulk flow, so it travels more slowly than the Bodipy dye. This difference in electrophoretic mobilities results in a separation of the two dyes into distinct analyte bands, as seen in Figures 6.16c and 6.16d. The zeta potential of the microchannel walls for the system used in this experiment was estimated at  $-50$  mV from the velocity of the neutral Bodipy dye [Bharadwaj and Santiago, 2000].

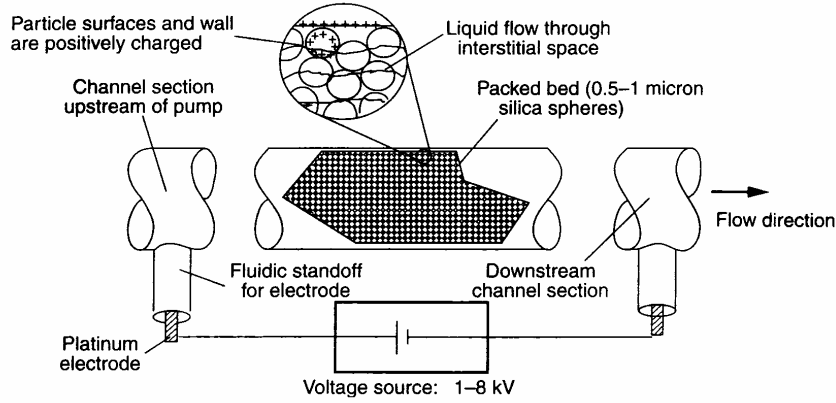
### 6.3.7 Engineering Considerations: Flowrate and Pressure of Electro-Osmotic Flow

As we have seen, the velocity field of systems with thin EDLs is approximately independent of the location in the microchannel and is therefore a “plug flow” profile for any cross section of the channel. The volume flow rate of such a flow is well approximated by the product of the electro-osmotic flow velocity and the cross-sectional area of the inner capillary:

$$Q = \frac{\epsilon \zeta EA}{\mu} \quad (6.59)$$

For the typical case of electrokinetic systems with a bulk ion concentration in excess of about  $100 \mu\text{M}$  and characteristic dimension greater than about  $10 \mu\text{m}$ , the vast majority of the current carried within the microchannel is the electromigration current of the bulk liquid. For such typical flows, we can rewrite the fluid flow rate in terms of the net conductivity of the solution,  $\sigma$ :

$$Q = -\frac{\varepsilon\zeta I}{\mu\sigma} \quad (6.60)$$



**FIGURE 6.17** Schematic of electrokinetic pump fabricated using a glass microchannel packed with silica spheres. The interstitial spaces of the packed bead structure create a network of submicron microchannels which can be used to generate pressures in excess of 5000 psi.

where  $I$  is the current consumed, and we have made the reasonable assumption that the electromigration component of the current flux dominates. The flow rate of a microchannel is therefore a function of the current carried by the channel and otherwise independent of geometry.

Another interesting case is that of an electrokinetic capillary with an imposed axial pressure gradient. For this case, we can use Eq. (6.47) to show the magnitude of the pressure that an electrokinetic microchannel can achieve. To this end, we solve Eq. (6.47) for the maximum pressure generated by a capillary with a sealed end and an applied voltage  $\Delta V$ , noting that the electric field and the pressure gradient can be expressed as  $\Delta V/L$  and  $\Delta p/L$ , respectively. Such a microchannel will produce zero net flow but will provide a significant pressure gradient in the direction of the electric field (in the case of a negatively charged wall). Imposing a zero net flow condition  $Q = \int_A \mathbf{u} \cdot d\mathbf{A} = 0$ , the solution for pressure generated in a thin EDL microchannel is then:

$$\Delta p = -\frac{8\varepsilon\zeta\Delta V}{a^2} \quad (6.61)$$

which shows that the generated pressure will be directly proportional to voltage and inversely proportional to the square of the capillary radius. Eq. (6.61) dictates that decreasing the characteristic radius of the microchannel will result in higher pressure generation. This principle has, for example, been demonstrated effectively by electrokinetic pumps that have been built recently [Paul et al., 1998a; Zeng et al., 2000]. Pressures in excess of 20 atm have been demonstrated. Figure 6.17 shows a schematic of one of these pumps. This structure achieves a network of submicron-diameter microchannels by packing 0.5- to 1- $\mu\text{m}$  spheres in fused silica capillaries, using the interstitial spaces in these packed beds as flow passages.



### 6.3.8 Electrical Analogy and Microfluidic Networks

There is a strong analogy between electro-osmotic and electrophoretic transport and resistive electrical networks of microchannels with long axial-to-radial-dimension ratios. As described above, the electro-osmotic flowrate is directly proportional to the current. This analogy holds provided that the previously described conditions for electric/velocity field similarity also hold. Therefore, Kirchoff's current and voltage laws can be used to predict flow rates in a network of electro-osmotic channels given voltage at endpoint "nodes" of the system. In this one-dimensional analogy, all of the current, and hence all of the flow entering a node, must also leave that node. The resistance of each segment of the network can be determined by knowing the cross-sectional area, the conductivity of the liquid buffer and the length of the segment. Once the resistances and applied voltages are known, the current and electro-osmotic flow rate in every part of the network can be determined using Eq. (6.60).

### 6.3.9 Practical Considerations

A few practical considerations should be considered in the design, fabrication and operation of electrokinetic microfluidic systems. These considerations include the dimensions of the system, the choice of liquid and buffer ions, the field strengths used and the characteristics of the flow reservoirs and interconnects. A few examples of these design issues are given here.

In the case of microchannels used to generate pressure, Eq. (6.60) shows that a low liquid conductivity is essential for increasing thermodynamic efficiency of an electrokinetic pump, as Joule heating is an important contributor to dissipation [Zeng et al., 2000]. In electrokinetic systems for chemical analysis, on the other hand, the need for a stable pH requires a finite buffer strength, and typical buffer strengths are in the 1- to 100-mM range. The need for a stable pH, therefore, often conflicts with a need for high fields to achieve high-efficiency separations because of the effects of Joule heating of the liquid.

Joule heating of the liquid in electrokinetic systems can be detrimental in two ways. First, temperature gradients within the microchannel cause a nonuniformity in the local mobility of electrophoretic particles because the local viscosity is a function of temperature. This nonuniformity in mobility results in a dispersion associated with the transport of electrophoretic species [Bosse and Arce, 2000; Grushka et al., 1989; Knox, 1988]. The second effect of Joule heating is the rise in the absolute temperature of the buffer. This temperature rise results in higher electro-osmotic mobilities and higher sample diffusivities. In microchip electrophoretic separations, the effect of increased diffusivity on separation efficiency is somewhat offset by the associated decrease in separation time. In addition, the authors have found that an important limitation to the electric field magnitude in microchannel electrokinetics is that the associated elevated temperatures and decreases in gas solubility of the solution often result in the nucleation of gas bubbles in the channel. This effect of driving gas out of solution typically occurs well before the onset of boiling and can be catastrophic to the electrokinetic system, as gas bubbles grow and eventually break the electrical circuit required to drive the flow. This effect can be reduced by outgassing of the solution and is, of course, a strong function of the channel geometry, buffer conductivity and the thermal properties of the substrate material.

Finally, an important consideration in electrokinetic experiments is the inadvertent application and/or generation of pressure gradients in the microchannel. Probably the most common cause of this is a mismatch in the height of the fluid level at the reservoirs. Note that, although there may not be a mismatch of fluid level at the start of an experiment, the flow rates created by electro-osmotic flow may eventually create a fluid level mismatch. Also, the fluid level in each reservoir, particularly in reservoirs of 1 mm diameter or less, may be affected by electrolytic gas generation at each electrode. Because electro-osmotic flowrate scales as channel diameter squared and pressure-driven flow scales as channel diameter to the fourth power, this effect is greatly reduced by decreasing the characteristic channel diameter. Another common method of reducing this pressure head effect is to increase the length of the channel for a given cross section. This length increase, of course, implies an increase in operating voltages to achieve the same flowrate. A second source of pressure gradients is a nonuniformity in the surface charge in the channel. An elegant, closed-form solution for the flow in a microchannel with arbitrary axial zeta potential distribution is presented by Anderson and Idol (1985). Recently, Herr et al. (2000) have

visualized this effect and offered a simple analytical expression to the pressure-driven flow components associated with zeta potential gradients in fully developed channel flows.

## 6.4 Summary and Conclusions

---

In microchannels, the flow of a liquid differs fundamentally from that of a gas, primarily due to the effects of compressibility and potential rarefaction in gases. Although significant differences from continuum macroscale theory have been reported, Sharp et al. (2000) have shown that in the range of accepted laminar flow behavior, the friction factor agrees with classical continuum hydrodynamic theory to within small or negligible differences. Transition to turbulence occurs at  $Re = 2000$  [Sharp et al., 2000].

However, large differences in observed pressure drop in microchannels have been reported by many investigators. These differences may be due to imperfections in the flow system of the experiment. Because imperfections may well occur in real engineering systems, it is essential to understand the sources of the observed discrepancies in order to avoid them, control them or factor them into the designs.

The development of measurement techniques for liquid flows is advancing quickly, both as macroscale methods are adapted to these smaller scales and as novel techniques are being developed. Further insight into phenomena present in the microscale flows, including those due to imperfections in channels or flow systems, is likely to occur rapidly given the evolving nature of the measurement techniques. Complex, nonlinear channels can be used efficiently to design for functionality.

Electrokinetics is a convenient and easily controlled method of achieving sample handling and separations on a microchip. Because the body force exerted on the liquid is limited to a region within a few nanometers from the wall, the resulting profiles, in the absence of imposed pressure gradients, are typically plug-like for channel dimensions greater than about  $10\ \mu\text{m}$  and ion concentrations greater than about  $10\ \mu\text{M}$ . For simple electro-osmotic flows with thin EDLs, low Reynolds number, uniform surface charge and zero imposed pressure gradients, the velocity field of these systems is well approximated by potential flow theory. This significant simplification can, in many cases, be used to predict and optimize the performance of electrokinetic systems. Further, electrokinetics can be used to generate large pressures ( $>20\ \text{atm}$ ) on a microfabricated device. In principle, the handling and rapid mixing of less than  $1\ \text{pL}$  of sample volumes should be possible using electrokinetic systems built with current microfabrication technologies.

## Nomenclature

---

$\delta$	lattice spacing
$\epsilon$	surface roughness or permittivity of liquid
$\phi$	local potential
$\kappa$	thermal diffusivity
$\lambda$	mean free path
$\lambda_D$	Debye length
$\mu$	dynamic viscosity
$\mu_r$	roughness viscosity
$\nu$	kinematic viscosity
$\nu_{\text{eph}}$	electrophoretic mobility
$\rho$	density
$\rho_E$	net charge density in EDL
$\sigma$	net conductivity of solution
$\tau$	time constant or characteristic time scale of a forcing function
$\tau_{ij}$	stress tensor
$\tau_w$	local wall shear stress
$\bar{\tau}_w$	wall shear stress, averaged around the perimeter
$\zeta$	zeta potential

$\Phi$	rate of conversion of mechanical energy to thermal energy (viscous dissipation function)
$a$	radius of cylindrical capillary, $=D/2$
$b_i$	body force per unit mass in the $i$ th direction
$\mathbf{b}$	body force per unit mass
$c_i$	Boltzmann distribution of ions of species $i$
$c_o$	proportionality constant
$c_p$	specific heat at constant pressure
$c_{\infty,i}$	molar concentration of ion $i$ in the bulk
$d$	Stokes diameter of the particle
$e$	charge of an electron
$f$	Darcy friction factor
$g_i$	gravitational acceleration in the $i$ th direction
$\mathbf{g}$	gravitational acceleration
$k$	thermal conductivity or Boltzmann's constant
$\mathbf{n}$	local unit vector
$p$	pressure
$\mathbf{q}$	heat flux
$q$	total molecule charge
$r$	radial coordinate
$t$	time
$u_{\text{crit}}$	critical velocity
$u_{\text{EOF}}$	electro-osmotic velocity
$u_i$	$i$ th component of velocity
$u_{\text{max}}$	maximum $u$ velocity
$u_{\text{particle}}$	total velocity of electrophoretic particles
$u_{\text{pressure}}$	pressure-driven velocity
$u_{\text{slip}}$	velocity evaluated at slip surface at the top of the EDL
$\mathbf{u}$	velocity vector
$x$	streamwise coordinate
$x_i$	coordinate in the $i$ th direction
$y$	coordinate perpendicular to the streamwise direction
$z$	coordinate perpendicular to the streamwise direction or valence number of the ion
$A$	cross-sectional area
$C_{\text{elec}}$	electrical capacitance
$C_{\text{flow}}$	capacitance of a fluid element
$C^*$	normalized friction coefficient
$D$	characteristic channel dimension (usually diameter)
$D_h$	hydraulic diameter
$E$	electric field driving the fluid
$E_{\text{slip}}$	electric field evaluated at slip surface at the top of the EDL
$F$	Faraday's constant
$H$	channel height
$I$	electrical current
$I_0$	zero-order modified Bessel function of the first kind
$K$	pressure drop parameter
$Kn$	Knudsen number
$L$	channel length
$L_s$	characteristic length scale
$L_e$	entrance length

$N_A$	Avogadro's number
$P$	perimeter
$Q$	flux
$PO$	Poiseuille number
$R_{\text{flow}}$	flow resistance
$R_{\text{elec}}$	electrical resistance
$Re$	Reynolds number
$Re_{\text{crit}}$	critical Reynolds number
$St$	Strouhal number
$T$	temperature
$U_s$	characteristic velocity scale
$\bar{U}$	area-averaged velocity
$V$	voltage
$V_1$	molar volume
$V_i$	time-dependent voltage applied to a reservoir "well"
$W$	channel width
STP	standard temperature and pressure

## References

- Adamson, A.W., and Gast, A.P. (1997) *Physical Chemistry of Surfaces*, sixth edition, John Wiley & Sons, New York.
- Alarie, J.P., Jacobson, S.C., Culbertson, C.T. et al. (2000) "Effects of the Electric Field Distribution on Microchip Valving Performance," *Electrophoresis* **21**, pp. 100–106.
- Anderson, J.L., and Idol, W.K. (1985) "Electroosmosis Through Pores with Nonuniformly Charged Walls," *Chem. Eng. Commun.* **38**, pp. 93–106.
- Arkilic, E.B., Schmidt, M.A., and Breuer, K.S. (1997) "Gaseous Slip Flow in Long Microchannels," *J. MEMS* **6**, pp. 167–178.
- Baker, D.R. (1995) *Capillary Electrophoresis*, Techniques in Analytical Chemistry Series, John Wiley & Sons, New York.
- Bharadwaj, R., and Santiago, J.G. (2000) unpublished results, Stanford University, Stanford, CA.
- Bianchi, F., Ferrigno, R., and Girault, H.H. (2000) "Finite Element Simulation of an Electroosmotic-Driven Flow Division at a T-Junction of Microscale Dimensions," *Anal. Chem.* **72**, pp. 1987–1993.
- Bosse, M.A., and Arce, P. (2000) "Role of Joule Heating in Dispersive Mixing Effects in Electrophoretic Cells: Convective-Diffusive Transport Aspects," *Electrophoresis* **21**, pp. 1026–1033.
- Brandner, J., Fichtner, M., Schygulla, U., and Schubert, K. (2000) "Improving the Efficiency of Micro Heat Exchangers and Reactors," in *Proc. 4th Int. Conf. Microreaction Technology, AIChE*, March 5–9, Atlanta, GA, pp. 244–249.
- Branbjerg, J., Fabius, B., and Gravesen, P. (1995) "Application of Miniature Analyzers: From Microfluidic Components to  $\mu$ TAS," in *Micro Total Analysis Systems*, eds. A. van den Berg and P. Bergveld, Kluwer Academic, Dordrecht, pp. 141–151.
- Branbjerg, J., Gravesen, P., Krog, J.P., and Nielsen, C.R. (1996) "Fast Mixing by Lamination," in *Proc. 9th Annual Workshop of Micro Electro Mechanical Systems*, February 11–15, San Diego, CA, pp. 441–446.
- Bridgman, P.W. (1923) "The Thermal Conductivity of Liquids Under Pressure," *Proc. Am. Acad. Arts Sci.* **59**, pp. 141–169.
- Brody, J.P., Yager, P., Goldstein, R.E., and Austin, R.H. (1996) "Biotechnology at Low Reynolds Numbers," *Biophys. J.* **71**, pp. 3430–3441.
- Burgreen, D., and Nakache, F.R. (1964) "ElectroKinetic Flow in Ultrafine Capillary Slits," *J. Phys. Chem.* **68**, pp. 1084–1091.
- Chen, Z., Milner, T.E., Dave, D., and Nelson, J.S. (1997) "Optical Doppler Tomographic Imaging of Fluid Flow Velocity in Highly Scattering Media," *Opt. Lett.* **22**, pp. 64–66.

- Choi, S.B., Barron, R.F., and Warrington, R.O. (1991) "Fluid Flow and Heat Transfer in Microtubes," in *DSC-Vol. 32, Micromechanical Sensors, Actuators and Systems*, ASME Winter Annual Meeting, Atlanta, GA, pp. 123–134.
- Cummings, E.B., Griffiths, S.K., and Nilson, R.H. (1999) "Irrotationality of Uniform Electroosmosis," in *SPIE Conf. on Microfluidic Devices and Systems II*, Santa Clara, CA, **3877**, pp. 180–189.
- Cummings, E.B., Griffiths, S.K., Nilson, R.H. et al. (2000) "Conditions for Similitude between the Fluid Velocity and Electric Field in Electroosmotic Flow," *Anal. Chem.* **72**, pp. 2526–2532.
- Devasenathipathy, S., and Santiago, J.G. (2000) unpublished results, Stanford University, Stanford, CA.
- Eringen, A.C. (1964) "Simple Microfluids," *Int. J. Eng. Sci.* **2**, pp. 205–217.
- Flockhart, S.M., and Dhariwal, R.S. (1998) "Experimental and Numerical Investigation into the Flow Characteristics of Channels Etched in <100> Silicon," *J. Fluids Eng.* **120**, pp. 291–295.
- Gad-el-Hak, M. (1999) "The Fluid Mechanics of Microdevices—The Freeman Scholar Lecture," *J. Fluids Eng.* **121**, pp. 5–33.
- Galambos, P., and Forster, F.K. (1998) "Micro-Fluidic Diffusion Coefficient Measurement," in *Micro Total Analysis Systems*, eds. D.J. Harrison and A. van den Berg, Kluwer Academic, Dordrecht, pp. 189–192.
- Grushka, E., McCormick, R.M., and Kirkland, J.J. (1989) "Effect of Temperature Gradients on the Efficiency of Capillary Zone Electrophoresis Separations," *Anal. Chem.* **61**, pp. 241–246.
- Hagen, G. (1839) "On the Motion of Water in Narrow Cylindrical Tubes [German]," *Pogg. Ann.* **46**, p. 423.
- Harley, J.C., Huang, Y., Bau, H.H., and Zemel, J.N. (1995) "Gas Flow in Micro-Channels," *J. Fluid Mech.* **284**, pp. 257–274.
- Hayes, M., Khetarpal, I., and Ewing, A. (1993) "Effects of Buffer pH on Electroosmotic Flow Control by an Applied Radial Voltage for Capillary Zone Electrophoresis," *Anal. Chem.* **65**, pp. 27–31.
- Henry, D.C. (1948) "The Electrophoresis of Suspended Particles. IV. The Surface Conductivity Effect," *Trans. Faraday Soc.* **44**, pp. 1021–1026.
- Herr, A.E., Molho, J.I., Santiago, J.G. et al. (2000) "Electroosmotic Capillary Flow with Nonuniform Zeta Potential," *Anal. Chem.* **72**, pp. 1053–1057.
- Hiemenz, P.C., and Rajagopalan, R. (1997) *Principles of Colloid and Surface Chemistry*, third edition, Marcel Dekker, New York.
- Hitt, D.L., and Lowe, M.L. (1999) "Confocal Imaging of Flows in Artificial Venular Bifurcations," *Trans. ASME J. Biomech. Eng.* **121**, pp. 170–177.
- Huang, T., Tsai, P., Wu, Ch., and Lee, C. (1993) "Mechanistic Studies of Electroosmotic Control at the Capillary-Solution Interface," *Anal. Chem.* **65**, pp. 2887–2893.
- Hunter, R.J. (1981) *Zeta Potential in Colloid Science*, Academic Press, London.
- Israelachvili, J.N. (1986) "Measurement of the Viscosity of Liquids in Very Thin Films," *J. Coll. Interface Sci.* **110**, pp. 263–271.
- Jacobson, S.C., Hergenroder, R., Moore, A.W., Jr., and Ramsey, J.M. (1994) "Precolumn Reactions with Electrophoretic Analysis Integrated on a Microchip," *Anal. Chem.* **66**, pp. 4127–4132.
- Janson, S.W., Helvajian, H., and Breuer, K. (1999) "MEMS, Microengineering and Aerospace Systems," in *30th AIAA Fluid Dyn. Conf.*, June 28–July 1, Norfolk, VA, AIAA 99-3802.
- Jiang, X.N., Zhou, Z.Y., Yao, J., Li, Y., and Ye, X.Y. (1995) "Micro-Fluid Flow in Microchannel," in *Transducers '95: Eurosensor IX*, 8th Int. Conf. on Solid-State Sensors and Actuators and Eurosensors IX, Sweden, pp. 317–320.
- Khaledi, M.G. (1998) "High-Performance Capillary Electrophoresis," in *Chemical Analysis: A Series of Monographs on Analytical Chemistry and its Applications*, Vol. 146, ed. J.D. Winefordner, John Wiley & Sons, New York.
- Kitahara, A., and Watanabe, A. (1984) *Electrical Phenomena at Interfaces: Fundamentals, Measurements, and Applications*, Vol. 15, Surfactant Science Series, Marcel Dekker, New York.
- Knox, J.H., (1988) "Thermal Effects and Band Spreading in Capillary Electro-Separation," *Chromatographia* **26**, pp. 329–337.
- Koutsiaris, A.G., Mathioulakis, D.S., and Tsangaris, S. (1999) "Microscope PIV for Velocity-Field Measurement of Particle Suspensions Flowing Inside Glass Capillaries," *Meas. Sci. Technol.* **10**, pp. 1037–1046.

- Lanzillotto, A.-M., Leu, T.-S., Amabile, M., and Wildes, R. (1996) "An Investigation of Microstructure and Microdynamics of Fluid Flow in MEMS," in *AD-Vol. 52, Proc. of ASME Aerospace Division*, Atlanta, GA, pp. 789–796.
- Liu, R.H., Stremmer, M.A., Sharp, K.V., Olsen, M.G., Santiago, J.G., Adrian, R.J., Aref, H., and Beebe, D.J. (2000) "Passive Mixing in a Three-Dimensional Serpentine Microchannel," *J. MEMS* **9**, pp. 190–197.
- Mala, G.M. (1999) "Heat Transfer and Fluid Flow in Microchannels," Ph.D. thesis, University of Alberta.
- Mala, G.M., and Li, D. (1999) "Flow Characteristics of Water in Microtubes," *Int. J. Heat Fluid Flow* **20**, pp. 142–148.
- Manz, A., Effenhauser, C.S., Burggraf, N. et al. (1994) "Electroosmotic Pumping and Electrophoretic Separations for Miniaturized Chemical Analysis Systems," *J. Micromech. Microeng.* **4**, pp. 257–265.
- Manz, B., Stilbs, P., Jönsson, B., Söderman, O., and Callaghan, P.T. (1995) "NMR Imaging of the Time Evolution of Electroosmotic Flow in a Capillary," *J. Phys. Chem.* **99**, pp. 11297–11301.
- Meinhart, C.D., Wereley, S.T., and Santiago, J.G. (1999) "PIV Measurements of a Microchannel Flow," *Exp. Fluids* **27**, pp. 414–419.
- Merkle, C.L., Kubota, T., and Ko, D.R.S. (1974) "An Analytical Study of the Effects of Surface Roughness on Boundary-Layer Transition," AF Office of Scientific Research, Space and Missile Sys. Org., AD/A004786.
- Molho, J.I., Herr, A.E., Mosier, B.P., Santiago, J.G., Kenny, T.W., Brennen, R.A., and Gordon, G. (2000) "Designing Corner Compensation for Electrophoresis in Compact Geometries," in *Micro Total Analysis Systems*, eds. A. van den Berg, W. Olthuis, and P. Bergveld, Kluwer Academic, Dordrecht, pp. 287–290.
- Novotny, E.J., and Eckert, R.E. (1974) "Rheological Properties of Viscoelastic Fluids from Continuous Flow Through a Channel Approximating Infinite Parallel Plates," *Trans. Soc. Rheol.* **18**, pp. 1–26.
- Overbeek, J.T.G. (1952a) "Electrochemistry of the Double Layer," in *Colloid Science*, ed. H.R. Kruyt, Elsevier, Amsterdam, pp. 115–277.
- Overbeek, J.T.G. (1952b) "Electrokinetic Phenomena," in *Colloid Science*, Vol. 1, ed. H.R. Kruyt, Elsevier, Amsterdam.
- Ovryn, B. (1999) "Three-Dimensional Forward Scattering Particle Image Velocimetry in a Microscopic Field-of-View," in *Proc. 3rd Int. Workshop PIV*, Sept. 16–18, Santa Barbara, CA, pp. 385–393.
- Papautsky, I., Brazzle, J., Ameel, T., and Frazier, A.B. (1999a) "Laminar Fluid Behavior in Microchannels Using Micropolar Fluid Theory," *Sensors and Actuators A* **73**, pp. 101–108.
- Papautsky, I., Gale, B.K., Mohanty, S., Ameel, T.A., and Frazier, A.B. (1999b) "Effects of Rectangular Microchannel Aspect Ratio on Laminar Friction Constant," in *SPIE Conf. on Microfluidic Devices and Systems II*, Santa Clara, CA, **3877**, pp. 147–158.
- Patankar, N.A., and Hu, H.H. (1998) "Numerical Simulation of Electroosmotic Flow," *Anal. Chem.* **70**, pp. 1870–1881.
- Paul, P.H., Arnold, D.W., and Rakestraw, D.J. (1998a) "Electrokinetic generation of high pressures using porous microstructures," in *Micro Total Analysis Systems*, ed. D.J. Harrison and A. van den Berg, Kluwer Academic, Dordrecht, pp. 49–52.
- Paul, P.H., Garguilo, M.G., and Rakestraw, D.J. (1998b) "Imaging of Pressure- and Electrokinetically Driven Flows Through Open Capillaries," *Anal. Chem.* **70**, pp. 2459–2467.
- Peng, X.F., Peterson, G.P., and Wang, B.X. (1994) "Frictional Flow Characteristics of Water Flowing Through Rectangular Microchannels," *Exp. Heat Transfer* **7**, pp. 249–264.
- Pfahler, J., Harley, J., Bau, H., and Zemel, J. (1990a) "Liquid Transport in Micron and Submicron Channels," *Sensors and Actuators A* **21–A23**, pp. 431–434.
- Pfahler, J., Harley, J., Bau, H.H., and Zemel, J. (1990b) "Liquid and Gas Transport in Small Channels," in *DSC-Vol. 19, Microstructures, Sensors and Actuators*, ASME Winter Annual Meeting, Dallas, TX, pp. 149–157.
- Pfahler, J., Harley, J., Bau, H., and Zemel, J.N. (1991) "Gas and Liquid Flow in Small Channels," in *DSC-Vol. 32, Micromechanical Sensors, Actuators and Systems*, ASME Winter Annual Meeting, Atlanta, GA, pp. 49–59.
- Poiseuille, M. (1840, 1841) "Recherches Expérimentales Sur le Mouvement des Liquides dans les Tubes de Très Petits Diamètres," *CR Hebdomaires des Séances Acad. Sci.* **11**.
- Prandtl, L., and Tietjens, O.G. (1934) *Applied Hydro- and Aeromechanics*, McGraw-Hill, New York.

- Probstein, R.F. (1994) *Physicochemical Hydrodynamics: An Introduction*, second edition, John Wiley & Sons, New York.
- Qu, W., Mala, G.M., and Li, D. (2000) "Pressure-Driven Water Flows in Trapezoidal Silicon Microchannels," *Int. J. Heat Mass Transfer* **43**, pp. 353–364.
- Reynolds, O. (1883) "An Experimental Investigation of the Circumstances Which Determine Whether the Motion of Water Will Be Direct or Sinuous, and the Law of Resistance in Parallel Channels," *Phil. Trans. R. Soc. London* **2**, p. 51.
- Rice, C.L., and Whitehead, R. (1965) "Electrokinetic Flow in a Narrow Cylindrical Capillary," *J. Phys. Chem.* **69**, pp. 4017–4024.
- Russel, W.B., Saville, D.A., and Schowalter, W.R. (1999) *Colloidal Dispersions*, ed. G.K. Batchelor, Cambridge Monographs on Mechanics and Applied Mathematics, Cambridge University Press, Cambridge, U.K.
- Santiago, J.G. (2001) "Electroosmotic Flows in Microchannels with Finite Inertial and Pressure Forces," *Anal. Chem.* **73**, pp. 2353–2365.
- Santiago, J.G., Wereley, S.T., Meinhart, C.D., Beebe, D.J., and Adrian, R.J. (1998) "A Particle Image Velocimetry System for Microfluidics," *Exp. Fluids* **25**, pp. 316–319.
- Scales, P., Grieser, F., and Healy, T. (1992) "Electrokinetics of the Silica-Solution Interface: A Flat Plate Streaming Potential Study," *ACS J. Langmuir Surf. Colloids* **8**, pp. 965–974.
- Schaller, Th., Bolin, L., Mayer, J., and Schubert, K. (1999) "Microstructure Grooves with a Width Less Than 50  $\mu\text{m}$  Cut with Ground Hard Metal Micro End Mills," *Precision Eng.* **23**, pp. 229–235.
- Schulte, T.H., Bardell, R.L., and Weigl, B.H. (2000) "On-Chip Microfluidic Sample Preparation," *J. Lab. Autom.* **5**, p. 83.
- Shah, R.K., and London, A.L. (1978) "Laminar Flow Forced Convection in Ducts," in *Advances in Heat Transfer*, Suppl. 1, Academic Press, New York.
- Sharp, K.V., Adrian, R.J., and Beebe, D.J. (2000) "Anomalous Transition to Turbulence in Microtubes," in *Proc. Int. Mech. Eng. Cong. Expo., 5th Micro-Fluidic Symp.*, Nov. 5–10, Orlando, FL, in press.
- Smoluchowski, M.V. (1903) "Contribution à la théorie de l'endosmose électrique et de quelques phénomènes corrélatifs," *Bull. Int. Acad. Sci. Cracovie* **8**, pp. 182–200.
- Taylor, J.A., and Yeung, E.S. (1993) "Imaging of Hydrodynamic and Electrokinetic Flow Profiles in Capillaries," *Anal. Chem.* **65**, pp. 2928–2932.
- Tieu, A.K., Mackenzie, M.R., and Li, E.B. (1995) "Measurements in Microscopic Flow with a Solid-State LDA," *Exp. Fluids* **19**, pp. 293–294.
- Tuckerman, D.B., and Pease, R.F.W. (1981) "High-Performance Heat Sinking for VLSI," *IEEE Electron Device Lett.* **EDL-2**, pp. 126–129.
- Webb, A., and Maynes, D. (1999) "Velocity Profile Measurements in Microtubes," in *30th AIAA Fluid Dyn. Conf.*, June 28–July 1, Norfolk, VA, AIAA 99-3803.
- Weigl, B.H., and Yager, P. (1999) "Microfluidic Diffusion-Based Separation and Detection," *Science* **283**, pp. 346–347.
- White, F.M. (1991) *Viscous Fluid Flow*, second edition, eds. J.P. Holman and J.R. Lloyd, McGraw-Hill, New York.
- White, F. M. (1994) *Fluid Mechanics*, third edition, McGraw-Hill, New York.
- Wilding, P., Pfahler, J., Bau, H.H., Zemel, J.N., and Kricka, L.J. (1994) "Manipulation and Flow of Biological Fluids in Straight Channels Micromachined in Silicon," *Clin. Chem.* **40**, pp. 43–47.
- Wu, P., and Little, W.A. (1983) "Measurement of Friction Factors for the Flow of Gases in Very Fine Channels Used for Microminiature Joule-Thomson Refrigerators," *Cryogenics* **23**, pp. 273–277.
- Yazdanfar, S., Kulkarni, M.D., and Izatt, J.A. (1997) "High Resolution Imaging of In Vivo Cardiac Dynamics Using Color Doppler Optical Coherence Tomography," *Opt. Exp.* **1**, pp. 424–431.
- Yu, D., Warrington, R., Barron, R., and Ameel, T. (1995) "An Experimental and Theoretical Investigation of Fluid Flow and Heat Transfer in Microtubes," in *Proc. of ASME/JSME Thermal Engineering Joint Conf.*, March 19–24, Maui, HI, pp. 523–530.
- Zeng, S., Chen, C., Mikkelsen, J.C. et al. (2000) "Fabrication and Characterization of Electrokinetic Micro Pumps," in *7th Intersoc. Conf. on Thermal and Thermomechanical Phenomena in Electronic Systems*, May 23–26, Las Vegas, NV.